Annu. Rev. Phys. Chem. 2004. 55:159–96
doi: 10.1146/annurev.physchem.55.091602.094416

First published online as a Review in Advance on February 3, 2004

FUNCTIONAL OXIDE NANOBELTS: Materials, Properties and Potential Applications in Nanosystems and Biotechnology

Zhong Lin Wang
School of Materials Science and Engineering, Georgia Institute of Technology, Atlanta, Georgia 30332-0245; email: zhong.wang@mse.gatech.edu

Key Words nanosensor, field effect transistor, nanocantilever, nanoresonator, nanospring, nanoring, piezoelectric nanobelt

■ **Abstract** Nanobelt is a quasi-one-dimensional structurally controlled nanomaterial that has well-defined chemical composition, crystallographic structure, and surfaces (e.g., growth direction, top/bottom surface, and side surfaces). This article reviews the nanobelt family of functional oxides, including ZnO, SnO_2, In_2O_3, Ga_2O_3, CdO, and PbO_2 and the relevant hierarchical and complex nanorods and nanowires that have been synthesized by a solid-vapor process. The nanobelts are single crystalline and dislocation free, and their surfaces are atomically flat. The oxides are semiconductors that have been used for fabrication of nanosize functional devices of key importance for nanosystems and biotechnology, such as field-effect transistors, gas sensors, nanoresonators, and nanocantilevers.

The structurally controlled ZnO nanobelts that exhibit piezoelectric properties are also reviewed. By controlling growth kinetics, we show the success of growing nanobelt-based novel structures whose surfaces are dominated by the polarized $\pm(0001)$ facets. Owing to the positive and negative ionic charges on the zinc- and oxygen-terminated $\pm(0001)$ surfaces, respectively, a spontaneous polarization is induced across the nanobelt thickness. As a result, helical nanostructures and nanorings are formed by rolling up single-crystal nanobelts; this phenomenon is a consequence of minimizing the total energy contributed by spontaneous polarization and elasticity. The polar surface–dominated ZnO nanobelts are likely to be an ideal system for understanding piezoelectricity and polarization-induced ferroelectricity at nano-scale and they could have applications as one-dimensional nano-scale sensors, transducers, and resonators.

INTRODUCTION

One of the most important contributions made by carbon nanotubes is having stimulated scientists' interest in one-dimensional nanostructures. Various techniques have been practiced in order to invent a variety of quasi-one-dimensional nanostructures (1, 2), the geometrical shapes of which include tubes (3, 4), cages (5–7),

cylindrical wires (8–12) and rods (13–15), nails (16), coaxial (17) and bi-axial cables (18), ribbons or belts (19, 20), sheets (21), diskettes (22), and more. Exploration of nanostructures that exhibit functionality is the key to nanotechnology. Functional oxides are the fundamental ingredients of smart systems, because the physical and chemical properties of the oxides can be tuned and controlled through adjusting cation valence state and anion deficiency (23). The structures of functional oxides are very diverse and colorful, and there are endless new phenomena and applications. Such unique characteristics have made oxides the most diverse class of materials, with properties covering almost all aspects of condensed matter physics and solid state chemistry in areas including semiconductivity, superconductivity, ferroelectricity, magnetism, and piezoelectricity.

Since the first discovery of semiconducting oxide nanobelts in our laboratory (19), investigation of oxide nanostructures has attracted considerable attention. The discovery of nanobelts is being attributed to the same category as the discovery of nanotubes (24) and it will stimulate a vast interest in investigating nanobelt-based materials and applications. There are about 1000 references on nanowire-related research; this paper reviews only the current progress in synthesis, property characterization, and device fabrication using oxide nanobelts. We first present the synthesis and structure of various oxide nanobelts. Then we discuss the growth mechanism, with the illustration of surface energy and growth kinetics. We demonstrate the applications of nanobelts as nanosize field-effect transistors (FETs), nanosensors, nanocantilevers, and nanoresonators. Finally, we review the most recent progress in the synthesis of piezoelectric nanobelts and the relevant phenomena induced by surface polarization.

SYNTHESIS TECHNIQUE

The oxide nanobelts were synthesized by a solid-vapor process. In principle, the thermal evaporation technique is a simple process in which condensed or powder source material is vaporized at elevating temperature, and then the resultant vapor phase condenses at certain conditions (temperature, pressure, atmosphere, substrate, etc.) to form the desired product. The processes are usually conducted in a horizontal tube furnace, as shown in Figure 1, which is composed of an alumina tube, a rotary pump system, and a gas supply and control system. A view window is set up at the left end of the alumina tube, which is used to monitor the growth process. The right-hand end of the alumina tube is connected to the rotary pump. Both ends are sealed by rubber O-rings. The ultimate vacuum for this configuration is $\sim 2 \times 10^{-3}$ Torr. The carrying gas comes in from the left end of the alumina tube and is pumped out at the right end. The source material is loaded on an alumina boat and positioned at the center of the alumina tube, where the temperature is the highest. Alumina substrates were placed downstream for collecting growth products. This simple setup can achieve high control of the final product.

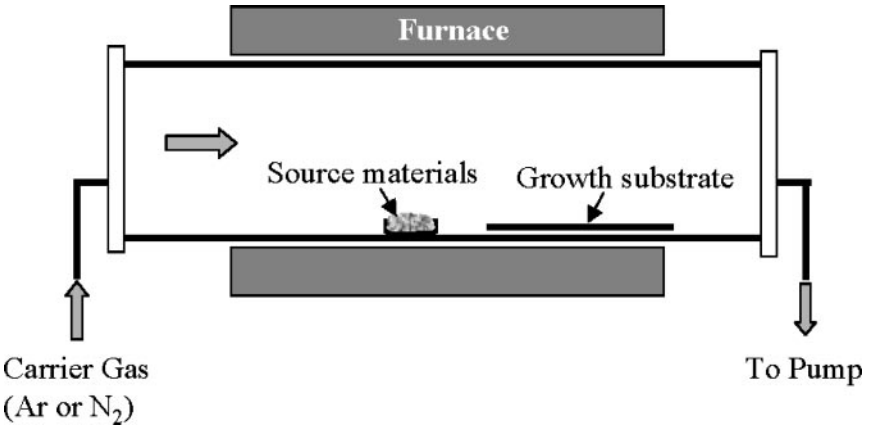

Figure 1 Schematic diagram of experimental apparatus for growth of oxide nanostructures.

There are several processing parameters such as temperature, pressure, carrier gas (including gas species and its flow rate), substrate, and evaporation time period that can be controlled and need to be selected properly before or during the thermal evaporation. The source temperature selection mainly depends on volatility of the source material. Usually, it is slightly lower than the melting point of the source material. The pressure is determined according to the evaporation rate or vapor pressure of source material. The substrate temperature usually drops with increasing distance from the position of source material. The local temperature determines the type of product to be received. It is also noted that the thermal evaporation process is very sensitive to the concentration of oxygen in the growth system. Oxygen influences not only the volatility of the source material and the stoichiometry of the vapor phase, but also the formation of product. After evacuating the alumina tube to $\sim 2 \times 10^{-3}$ Torr, thermal evaporation was conducted at a certain temperature for 2 h under a pressure of 200–600 Torr and an Ar carrier gas of 50 sccm (standard cubic centimeters per minute). The on and off time as well as the length of inletting the carrier gas could greatly affect the growth kinetics.

THE FAMILY OF NANOBELTS

Nanobelts Versus Nanowires

It is well known that a single-wall carbon nanotube can be metallic or semiconductor depending on the helical angle at which the graphitic sheet is rolled up. It is expected that the properties of a nanowire could be strongly affected by the structure of the side surfaces, analogous to the helical angle for carbon nanotubes,

which determines its electronic structure. In the literature there are a few names being used for describing one-dimensionally elongated structures, such as nanorod, nanowire, nanoribbon, nanofiber, and nanobelts. When we named the nanostructures "nanobelts" (19), we meant that the nanostructure has specific growth direction and the top, bottom, and side surfaces are well-defined crystallographic facets. The requirements for nanowires are less restrictive than those for nanobelts because a wire has a specific growth direction, but its side surfaces may not be well defined, and its cross-section may not be uniform or specific in shape. Therefore, we believe that nanobelts are more structurally controlled objects than are nanowires; or simply, a nanobelt is a nanowire that has well-defined side surfaces. It is well known that the physical property of a carbon nanotube is determined by the helical angle at which the graphite layer was rolled up. It is expected that the physical and chemical properties of thin nanobelts and nanowires will depend on the nature of the side surfaces.

A few kinds of nanobelts have been reported in the literature. Table 1 summarizes the nanobelt structures of function oxides. Each type of nanobelt is defined by its crystallographic structure, growth direction, top surfaces, and side surfaces. Some of the materials can grow along two directions, but they can be controlled experimentally. Although these materials belong to different crystallographic families, they do have a common faceted structure, which is the nanobelt structure. In addition, nanobelts of $Cu(OH)_2$ (25), MoO_3 (26, 27), MgO (28, 29), and CuO (30) have been successfully synthesized.

ZnO Nanobelts

In the family of nanobelts, ZnO is probably the most extensively studied structure. Thermal evaporation of ZnO powders (purity: 99.99%; melting point: 1975°C) at

TABLE 1 Crystallographic geometry of functional oxide nanobelts

Nanobelt	Crystal structure	Growth direction	Top surface	Side surface
ZnO	Wurtzite	[0001] or $[01\bar{1}0]$	$\pm(2\bar{1}\bar{1}0)$ or $\pm(2\bar{1}10)$	$\pm(01\bar{1}0)$ or $\pm(0001)$
Ga_2O_3	Monoclinic	[001] or [010]	$\pm(100)$ or $\pm(\bar{1}00)$	$\pm(010)$ or $\pm(\bar{1}01)$
t-SnO_2	Rutile	[101]	$\pm(10\bar{1})$	$\pm(010)$
o-SnO_2 wire	Orthorhombic	[010]	$\pm(100)$	$\pm(001)$
In_2O_3	C-rare earth	[001]	$\pm(100)$	$\pm(010)$
CdO	NaCl	[001]	$\pm(100)$	$\pm(010)$
PbO_2	Rutile	[010]	$\pm(201)$	$\pm(10\bar{1})$

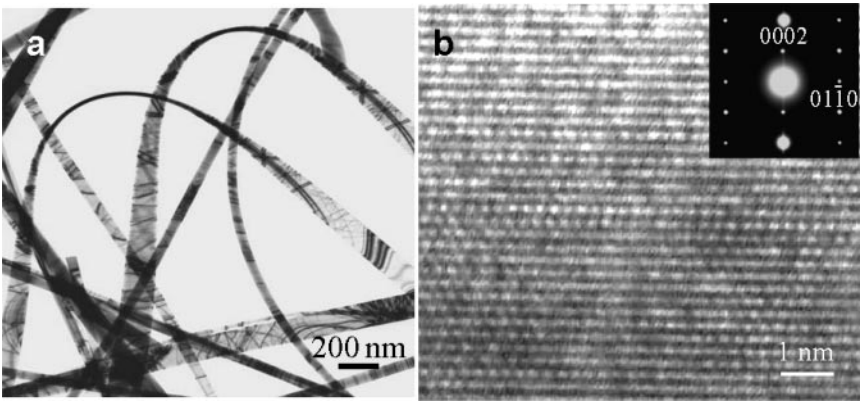

Figure 2 (*a*) Transmission electron microscopy (TEM) image of the as-synthesized ZnO nanobelts. (*b*) High-resolution TEM image recorded with the incident electron perpendicular to the top surface of the nanobelt.

1400°C resulted in ultralong ZnO nanobelts (Figure 2*a*). The typical lengths of the ZnO nanobelts are in the range of several tens to several hundreds of micrometers; some of them even have lengths on the order of millimeters. Energy-dispersive X-ray spectroscopy and X-ray diffraction measurements show that the sample is Wurtzite (hexagonal)–structured ZnO with a lattice constant of $a = 3.249$ Å and $c = 5.206$ Å, consistent with the standard values for bulk ZnO.

Transmission electron microscopy (TEM) images reveal that the geometrical shape of the ZnO nanobelts is distinct in cross section from the nanotubes or nanowires. Each nanobelt has a uniform width along its entire length, and the typical widths of the nanobelts are in the range of 50–300 nm. No particle was observed at the ends of the nanobelts. A ripple-like contrast that appeared in the TEM image is due to strain resulting from the bending of the belt. High-resolution TEM and electron diffraction studies show that the ZnO nanobelts are structurally uniform and single crystalline (Figure 2*b*).

SnO_2 Nanobelts

Single crystalline SnO_2 nanobelts of rutile structure were consistently synthesized by thermal evaporation of either SnO_2 powders (purity: 99.9%, melting point: 1630°C) at 1350°C or SnO powders (purity: 99.9%, melting point: 1080°C) at 1000°C (19, 31). TEM images (Figure 3*a*) display the characteristic shape of the SnO_2 nanobelts. High-resolution TEM images (Figure 3*b*) reveal that the nanobelts are single crystalline and dislocation free. Electron diffraction patterns indicate that the SnO_2 nanobelt grows along [101], and it is enclosed by $\pm(010)$ and $\pm(10\bar{1})$ crystallographic facets.

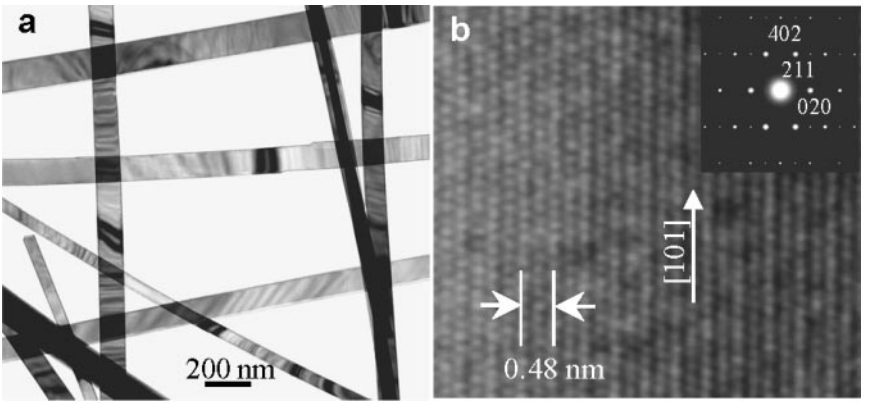

Figure 3 (*a*) Transmission electron microscopy (TEM) image of the as-synthesized SnO_2 nanobelts. (*b*) High-resolution TEM image recorded with the incident electron perpendicular to the top surface of the nanobelt.

In addition to the normal rutile-structured SnO_2, it has been possible to form an orthorhombic superlattice-like structure (32). The orthorhombic structure can form in a thin nanowire, coexist with the normal rutile-structured SnO_2 in a sandwiched nanoribbon, or occur in the form of nanotubes. This result is distinct from that for bulk SnO_2, where pressures in excess of 150 kbar are required to form the orthorhombic form. A comprehensive review of the SnO_2 and SnO-related nanostructures has been given elsewhere (33).

In_2O_3 Nanobelts

Nanobelts of In_2O_3 with C-rare earth crystal structure were also synthesized by our method (Figure 4). The evaporation of In_2O_3 powders (purity: 99.99%, melting point: $\sim$1920°C) at 1400°C yields In_2O_3 nanobelts. TEM observations show that most of the In_2O_3 nanobelts have uniform width and thickness along their lengths. Typically, the In_2O_3 nanobelts have widths in the range of 50–150 nm and lengths of several tens to several hundreds of micrometers. Electron diffraction analysis shows that the In_2O_3 nanobelts are single crystalline and grow along $\langle 100 \rangle$, the surfaces being enclosed by $\{100\}$. In_2O_3 nanobelts growing_along [120] type, with top and bottom surfaces (001) and side surface being [210] have also been observed (34). Transport properties of In_2O_3 nanobelts have also been reported (35).

CdO Nanobelts

Nanobelts of CdO with NaCl cubic structure were also synthesized by evaporating CdO powders (purity: 99.998%, melting point: 1430°C) at 1000°C (19). Besides

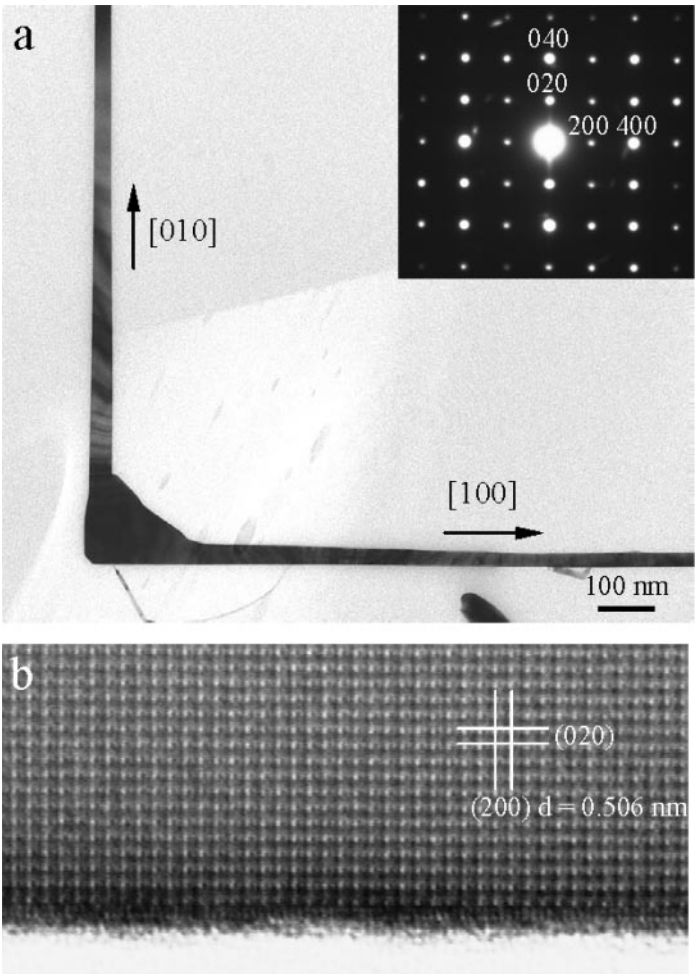

Figure 4 (*a*) Transmission electron microscopy (TEM) image of the as-synthesized L-shaped In_2O_3 nanobelts. The inset is the electron diffraction pattern recorded from the nanobelt. (*b*) High-resolution TEM image recorded with the incident electron perpendicular to the top surface of the nanobelt.

CdO nanobelts, many single crystalline CdO sheets with sizes on the order of several to several tens of micrometers were formed (Figure 5). These CdO sheets usually have shapes of rectangles, triangles, and parallelograms. The lengths of the CdO nanobelts are usually less than 100 μm, and their widths are typically 100–500 nm. Electron diffraction patterns show that the nanobelts grow along [100] and their surfaces are enclosed by $\pm(001)$ and $\pm(010)$ facets.

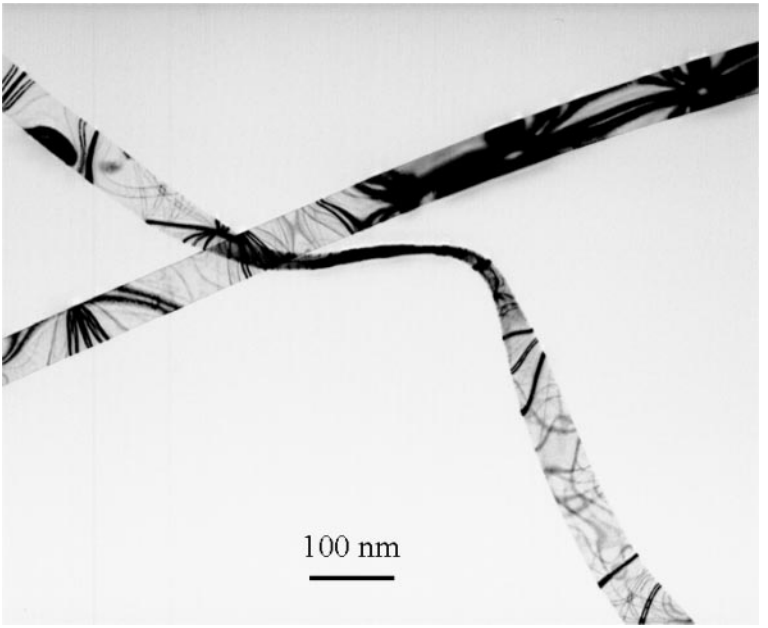

Figure 5 Transmission electron microscopy images of the as-synthesized CdO nanobelts.

Ga_2O_3 Nanobelts

Nanoribbons and flat nanosheets of Ga_2O_3 have been synthesized by evaporating GaN at high temperature in the presence of oxygen (36). The as-synthesized nanoribbons and nanosheets are pure, structurally uniform, single-crystalline and free from dislocations. The nanoribbons and nanosheets all have monoclinic β-Ga_2O_3 structure ($C2/m$, $a = 12.23$, $b = 3.04$, $c = 5.80$ Å, and $\beta = 103.7^\circ$). The flat top and bottom surfaces for both nanoribbons and nanosheets are $\pm(100)$ and the side surfaces are $\pm(010)$, and $\pm(10\bar{1})$ for nanoribbons and $\pm(010)$, $\pm(10\bar{1})$, and $\pm(21\bar{2})$ for nanosheets. The axis direction of nanoribbon growth is along either [001] or [010].

PbO_2 Nanobelts

β-PbO_2 nanobelts, with a rectangular cross section, a typical length of 10–200 μm, a width of 50–300 nm, and a width-to-thickness ratio of 5–10, have been successfully synthesized by evaporation of commercial PbO powders at high temperature (37). The PbO_2 nanobelts are enclosed by top surfaces $\pm(201)$ and side surfaces $\pm(10\bar{1})$, and their growth direction is [010]. Each PbO_2 nanobelt has a large polyhedral Pb tip at one of its ends, suggesting the growth is dominated by a vapor-liquid-solid mechanism. Electron beam irradiation of the

PbO_2 nanobelts results in the phase transformation from PbO_2 to PbO and finally to Pb.

ZnS Nanobelts

ZnS (zinc sulfide) has two types of crystal structures: hexagonal Wurtzite ZnS (referred to as the hexagonal phase) and cubic zinc blend ZnS (referred to as the cubic phase). Typically, the stable structure at room temperature is zinc blend, with few observances of stable Wurtzite ZnS. We have synthesized stable Wurtzite-structured nanobelts, nanocombs, and nanowindmills, using a simple catalyst-free thermal evaporation technique (38). Our synthesis technique is based on thermal evaporation of ZnS powders at elevated temperature. The as-synthesized sample is composed of several types of structures. The most typical structure observed is ZnS nanobelts (Figure 6). The nanobelts have a uniform cross section along their length, with a typical width of 2–30 μm and extend to over 100 μm in length. Electron diffraction indicates that all three types of structures are single crystalline with the Wurtzite ZnS structure ($a = 3.82$ Å, $c = 6.26$ Å). The comb-like, saw-toothed belts and the regular belt structures were found in the same growth-temperature range. The nanobelt grows along [0001], with side surfaces $(01\bar{1}0)$ and the top surfaces $(2\bar{1}10)$. Silicon-based nanobelts have also been reported (39).

HIERARCHICAL SUPERSTRUCTURES

Using a mixture of ZnO and SnO_2 powders in a weight ratio of 1:1 as the source material, a complex ZnO nanostructure was created (40). Figure 7*a* shows a low-magnification SEM image of the as-synthesized products with a uniform feature consisting of sets of central axial nanowires, surrounded by radial-oriented tadpole-like nanostructures. The morphology of the string appears like a liana, and the axial nanowire is the rattan, which has a uniform cross-section with dimension in the range of a few tens of nanometers. The tadpole-like branches have spherical balls at the tips (Figure 7*b*), and the branches display a ribbon shape. Energy-dispersive X-ray spectroscopy analysis shows that the tadpole-like structure and the central nanowire are ZnO, while the ball at the tip is Sn. The ribbon branches have a fairly uniform thickness, and their surfaces are rough with steps. The contact point between the nanoribbon with the axial nanowire is rather small, in the order of a few tens of nanometers, while far away from the contacting point the nanoribbon size is rather large, in the order of 100–200 nm.

In the synthesis, a mixture of SnO_2 and ZnO powders was used as the source material. SnO_2 can decompose into Sn and O_2 at high temperature; thus, the growth of the nanowire-nanoribbon junction arrays is the result of a vapor-liquid-solid growth process, in which the Sn catalyst particles are responsible for initiating and leading the growth of ZnO nanowires and nanoribbons. The growth of the novel structure presented here can be separated into two stages. The first stage is the fast growth of the ZnO axial nanowire along [0001]. The growth rate is so fast that a

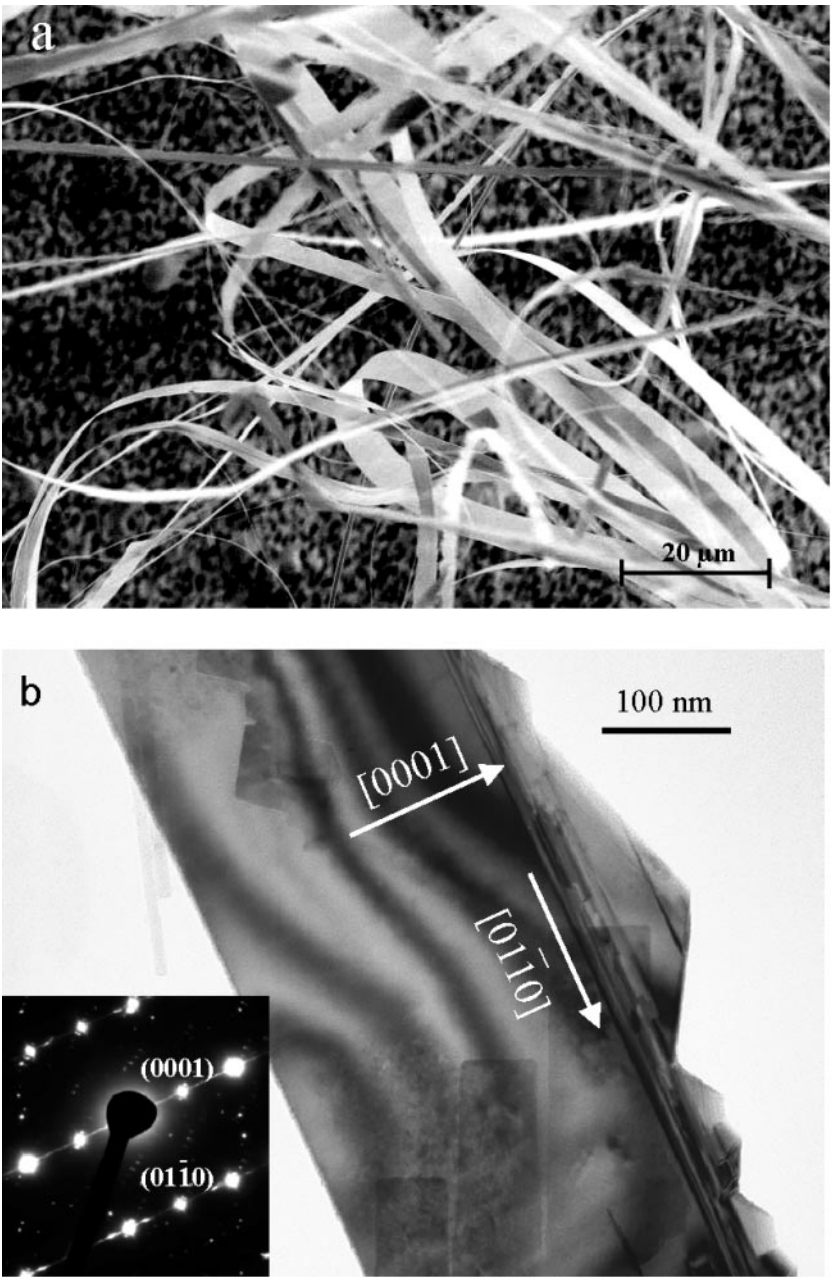

Figure 6 (*a*) Scanning electron microscopy (SEM) image of the as-synthesized ZnS nanobelts. (*b*) Transmission electron microscopy image of a ZnS nanobelt and the corresponding electron diffraction pattern (insert).

slow increase in the size of the Sn droplet has little influence on the diameter of the nanowire; thus, the axial nanowire has a fairly uniform shape along the growth direction. The second stage of growth is the nucleation and epitaxial growth of the nanoribbons owing to the arrival of tiny Sn droplets onto the ZnO nanowire surface. This stage is much slower than the first stage because the lengths of the nanoribbons are uniform and much shorter than those of the nanowire. Since Sn is in a liquid state at the growth temperature, it tends to adsorb the newly arriving Sn species and grow into a larger-sized particle (i.e., coalescing). Therefore, the width of the nanoribbon increases as the size of the Sn particle at the tip becomes larger, resulting in the formation of the tadpole-like structure observed in TEM (Figure 7*b*). The ZnO nanowire is likely to have a hexagonal cross section bounded by $\pm(10\bar{1}0)$, $\pm(01\bar{1}0)$ and $\pm(\bar{1}100)$, which are six crystallographic equivalent planes. The Sn liquid droplets deposited onto the ZnO nanowire lead to the simultaneous growth of the ZnO nanoribbons along the six growth directions: $\pm[10\bar{1}0]$, $\pm[0\bar{1}10]$, and $\pm[\bar{1}100]$ (Figure 7*c*). The angles between the two adjacent growth directions is 60°, resulting in the sixfold symmetric distribution of the nanoribbons around the nanowire.

Hierarchical structures of ZnO-In_2O_3 have also been synthesized (41). Using the flat surface of a nanobelt, a composite layered structure of two oxides has been grown, forming oxide-oxide or metal-oxide tape structures (42).

METAL NANOBELTS

Zn-ZnO core-shell nanbelts and nanotubes were synthesized with kinetic control (43). Pure ZnO powders were selected as the source material, which was loaded in an alumina boat and positioned at the center of a horizontal tube furnace. The silicon substrates for collecting the products were positioned at the low-temperature region of the furnace. The synthesis process has two steps. The first step is to control the evaporation and decomposition process, which was carried out by evacuating the alumina tube to $\sim 2 \times 10^{-3}$ torr and raising the temperature to 1350°C, keeping it there for 5 minutes, and not introducing a carrier gas. The second step is to control the growth, which was also carried out at 1350°C for 30 min but with the Ar carrier gas at a pressure of 200–250 torr and a flow rate of 25 sccm (standard cubic centimeters per minute). The substrate was placed downstream in the temperature region of 200–300°C.

TEM images illustrate that the Zn nanobelts have widths of ~50 nm (Figure 8*a*). Diffraction contrast across the structure suggests that it has a belt shape with a uniform thickness (the contrast presented in Figure 8*a* is due to the bending of the nanobelts along its length). Typical zigzag structures are frequently observed in the synthesized products. Dark-field images show that the ZnO covering on the top and bottom (0001) surfaces is of uniform thickness, while the ZnO on the side surfaces exhibits grainy structure (Figure 8*b*); however, the electron diffraction pattern (Figure 8*c*) recorded from the region indicates two sets of single-crystal diffraction spots, which are indexed as [0001] Zn and [0001] ZnO with an epitaxial

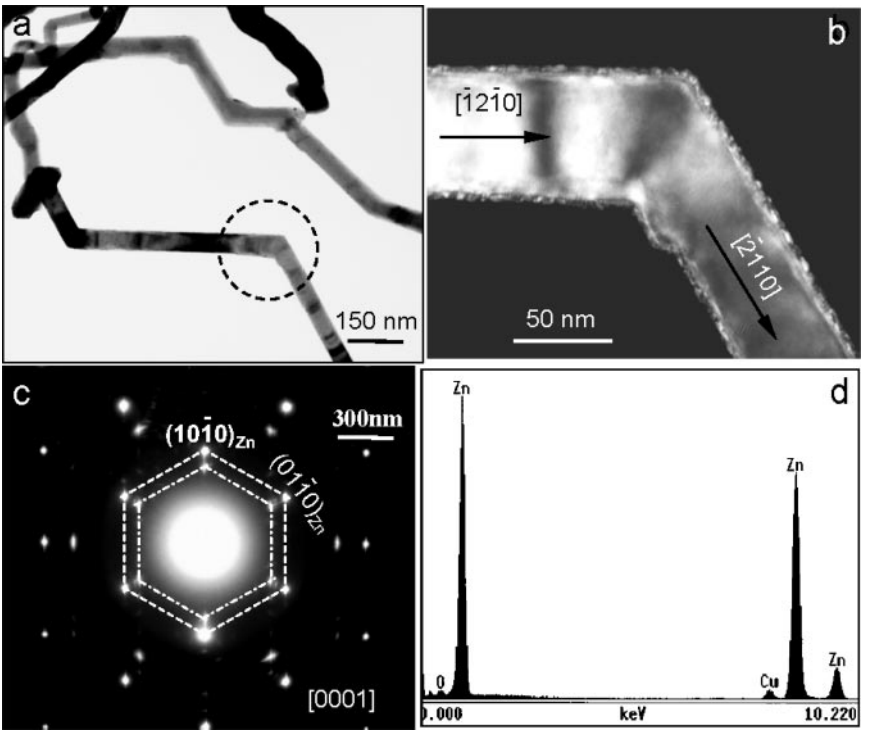

Figure 8 (*a*) Low-magnification transmission electron microscopy (TEM) image of the as-synthesized Zn nanobelts with zigzag structure. (*b*) A dark-field TEM image from the circled region in (*a*), showing uniform contrast across its width and the surface ZnO layer. (*c*) The corresponding [0001] electron diffraction pattern recorded from the circled region in (*a*), displaying the presence of ZnO on the surface of the Zn nanobelt. (*d*) Energy-dispersive X-ray spectroscopy spectrum recorded from the nanobelt, showing that the dominant element is Zn. The tiny Cu peak came from the TEM grid.

orientation. This type of composite nanobelt grows along $\langle 2\bar{1}\bar{1}0\rangle$, its top and bottom surfaces being (0001) and side surfaces $\{0\bar{1}10\}$. The zigzag structure presented in Figure 8*a* is due to a change in the growth direction from $[1\bar{2}10]$ to $[\bar{2}110]$, which are two crystallographically equivalent directions. A change in growth direction among the equivalent group of $\pm[2\bar{1}\bar{1}0]$, $\pm[\bar{1}2\bar{1}0]$, and $\pm[\bar{1}\bar{1}20]$ produces turning points in the growth directions. Energy dispersive X-ray spectroscopy shows that the nanobelt is dominated by Zn, with very little oxygen (Figure 8*d*). A detailed analysis of the interface of Zn core and ZnO shell has been given elsewhere (44).

Our synthesis experiment used ZnO powder as the raw material, while the produced products were Zn-ZnO core-shell nanobelts and ZnO nanobelts distributed

in distinct temperature regions. It is well known that the decomposition of ZnO occurs when it is subject to high enough temperature in vacuum. The thermodynamics of these processes can be presented as follows. The solid-vapor process and the decomposition process are expressed as

$$\mathrm{ZnO(s)} \leftrightarrow \mathrm{ZnO(g)} \tag{1}$$

$$\mathrm{ZnO(g)} \leftrightarrow \mathrm{Zn(g)} + {}^{1}/_{2}\mathrm{O_2(g)}. \tag{2}$$

The Zn nanobelt is formed by deposition of the Zn vapor at the low-temperature region, while the surface oxide layer is formed after forming the Zn nanobelt due to surface oxidation. Through a chemical approach, Ag nanoparticles can be transformed into nanobelts (45).

NANOBELTS AS TEMPLATES FOR SYNTHESIS OF NEW MATERIALS

Using the as-synthesized ZnO nanobelts as templates, nanostructured ZnS nanocables and nantubes have been synthesized by chemical reaction (46). Based on the geometrical shape of the nanobelt template, we anticipate to receive ZnS nanobelts based on the reaction

$$\mathrm{ZnO} + \mathrm{H_2S} \rightarrow \mathrm{ZnS} + \mathrm{H_2O}. \tag{3}$$

Figure 9 shows a comparison of the SEM images recorded from ZnO nanobelts before and after reacting with H_2S. Besides some particle-shape reaction products, nanobelts of ZnS have been formed, as indicated by arrowheads, but the nanobelts have pore sizes of ~30 nm. A rolled nanobelt is presented in the image, which is possibly produced by the surface tension introduced after the reaction; such a shape was rarely observed for the as-synthesized ZnO nanobelts. TEM analysis shows that the converted ZnS nanobelts have two types of structural configurations: rectangular ZnO-ZnS nanocables and ZnS nanotubes.

The conversion of ZnO nanobelts into ZnS nanocrystallite-structured nanocables and nanotubes occurrs in solution. Due to the limited solubility of ZnO in water, the reaction is essentially a substitution reaction; thus, the nanocable still preserves the rectangular cross section. The pores in the structures are produced because of two factors. The excess H_2O produced in the reaction may present in the structure and form the pores. From the structural point of view, ZnS has the zinc blende structure (cubic) with $a = 0.54{,}109$ nm, and ZnO has the Wurtzite structure (hexagonal) with $a = 0.3249$ nm and $c = 0.52{,}065$ nm; both are incompatible in structure. Thus, the substitution reaction is unlikely to produce single-crystalline ZnS. The formation of nanocrystallites is expected especially when the reaction temperature is at room temperature.

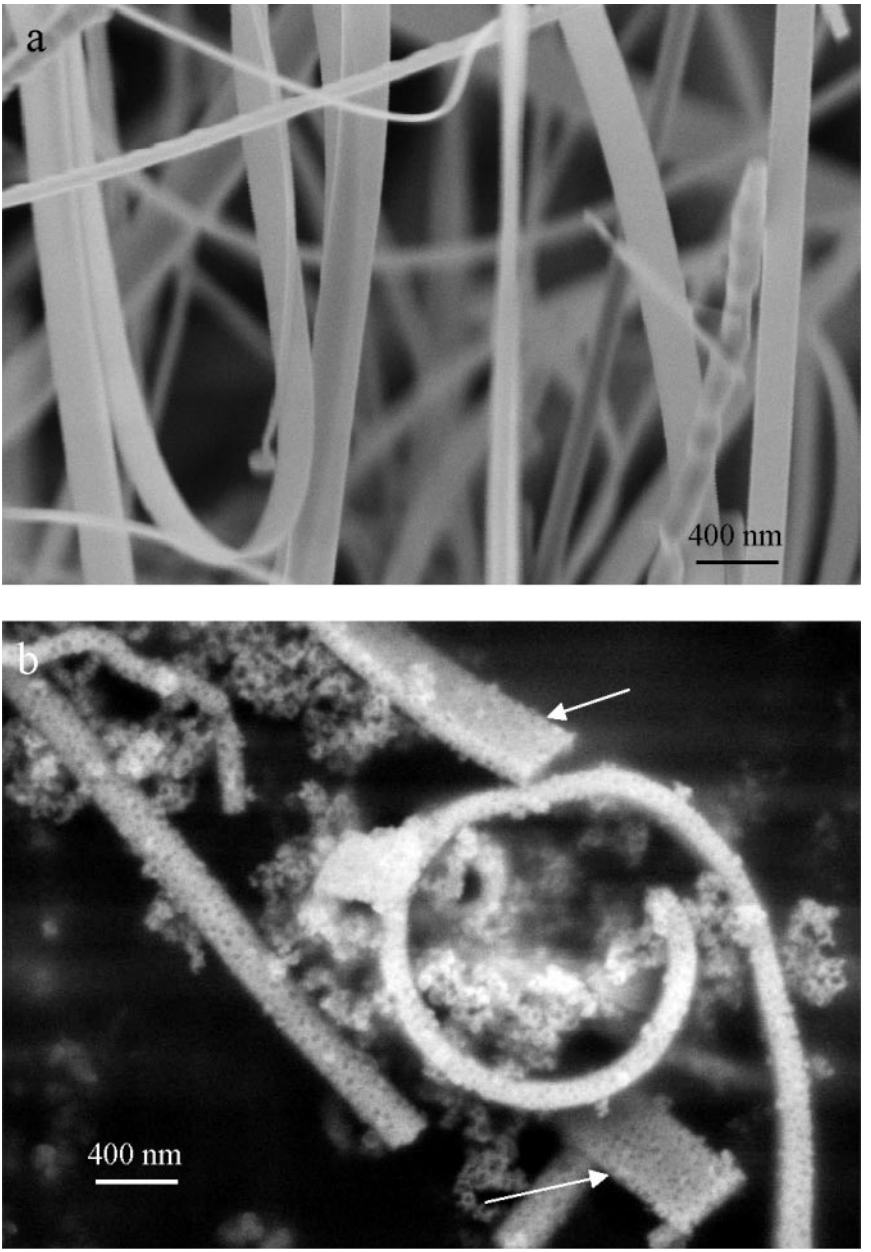

Figure 9 SEM images of (*a*) ZnO nanobelts and (*b*) the ZnS nanobelts converted through chemical reaction with H_2S.

SPIN-DOPED NANOBELTS FOR SPINTRONICS

Diluted magnetic semiconductors are one of the promising materials for spintronics (spin + electronics), a proposed technology that uses the electron spin rather than the electron charge for reading and writing information (47, 48). Much recent effort toward spintronics has been focused on the synthesis and characterization of manganese-doped III-V and II-VI materials, with prominent interest on GaN:Mn and ZnO:Mn due to a proposed and measured Curie temperature above room temperature (49). The integration of diluted magnetic semiconductor materials into today's electronics will require very low dimensions in order to make real use of the advantage offered by spin, but the majority of the recent studies are focused on bulk materials. Furthermore, for the future goal, a doping technique of nanosize structures has to be established offering precise control of the species in both concentration and lateral position.

We have used ion implantation to modify the electrical and optical properties of ZnO nanobelts, aiming at developing quasi-one-dimensional nanomaterial for spintronics (50). Ion implantation of $^{55}Mn^{+}$ ions into the ZnO nanobelts was carried out at room temperature with an ion energy of 30 keV and a flux of 1×10^{15} cm^{-2}. Figure 10 shows TEM images of the as-implanted ZnO nanobelt, displaying numerous stacking faults generated in the volume. High-resolution TEM images clearly reveal the fine details of the atomic lattice at the vicinity of the Mn ion–induced stacking faults. Damage at the surface of the nanobelt is also visible. We have found that annealing the sample at different temperatures can control the density of stacking faults, possibly resulting in tunable electrical and optical properties.

ALIGNED GROWTH OF ZnO NANORODS

Tin is an excellent catalyst for growth of ZnO nanostructures. Using tin as a catalyst, we have grown aligned ZnO nanowires on a polycrystalline alumina substrate. The SEM image shown in Figure 11*a* clearly displays the reasonable alignment among the nanowires. Higher magnification SEM images show that the nanowire has a nonuniform cross section along its length and it becomes sharper toward the tip. The very tip has a Sn-rich head (Figures 11*b*,*c*). Gold has been used for growth of aligned ZnO nanorods (51).

By using Sn particles reduced from SnO_2, well-aligned ZnO nanorods with identical crystallographic-orientation have been synthesized using a vapor-transport deposition process (52). Orientation-ordered nanorods grow normal to the c-planes of the as-deposited micron-sized ZnO rods on a polycrystalline Al_2O_3 substrate, and each nanorod is along [0001] and enclosed by $\{2110\}$ facet surfaces. The nanorods remain in identical crystal orientation with a homoepitaxial orientation relationship with the microrod. By controlling the growth time at high temperature, uniform lengths of aligned nanorods have been received.

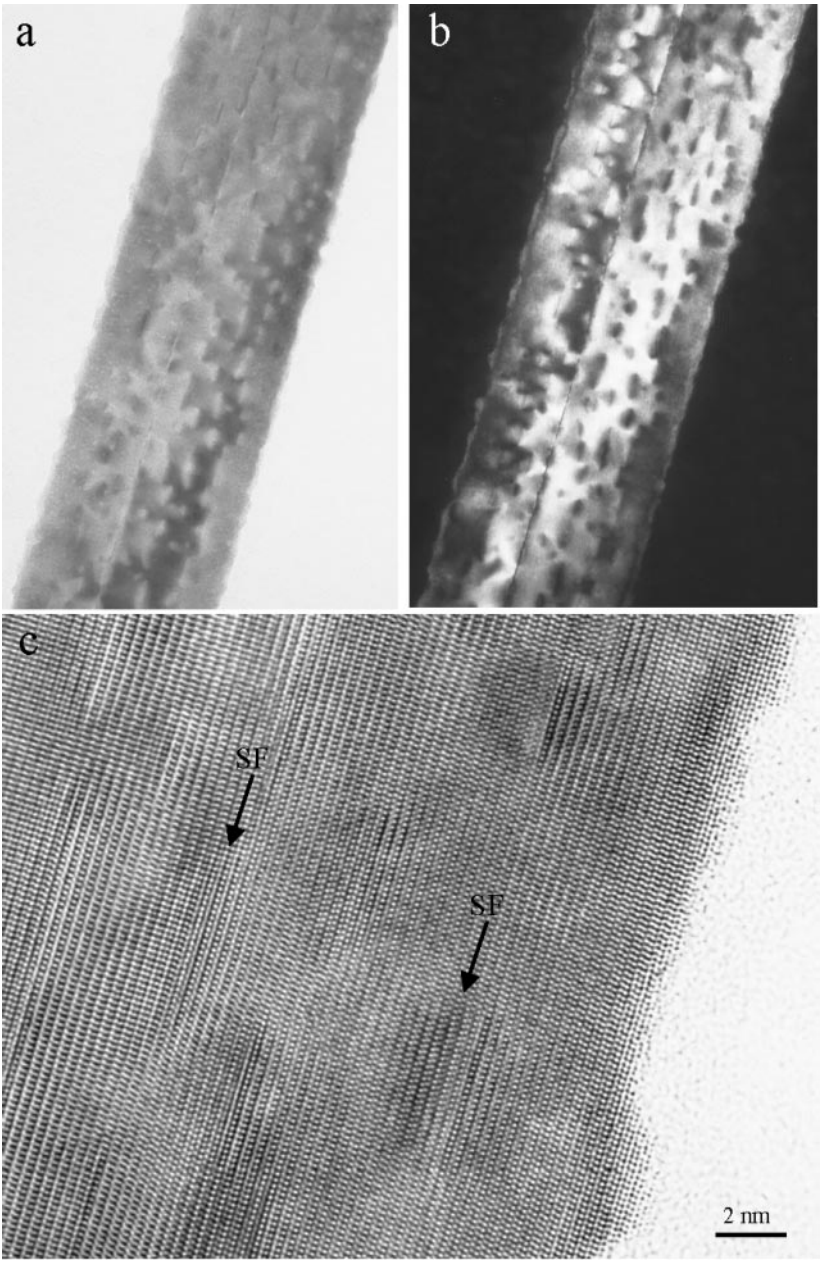

Figure 10 (*a*,*b*) Bright-field and dark-field TEM images of ZnO nanobelts doped with Mn. (*c*) High-resolution TEM image of the doped nanobelt, showing numerous mini stacking faults confined in the c-plane. The stacking fault terminated inside the nanobelt with the creation of partial dislocations.

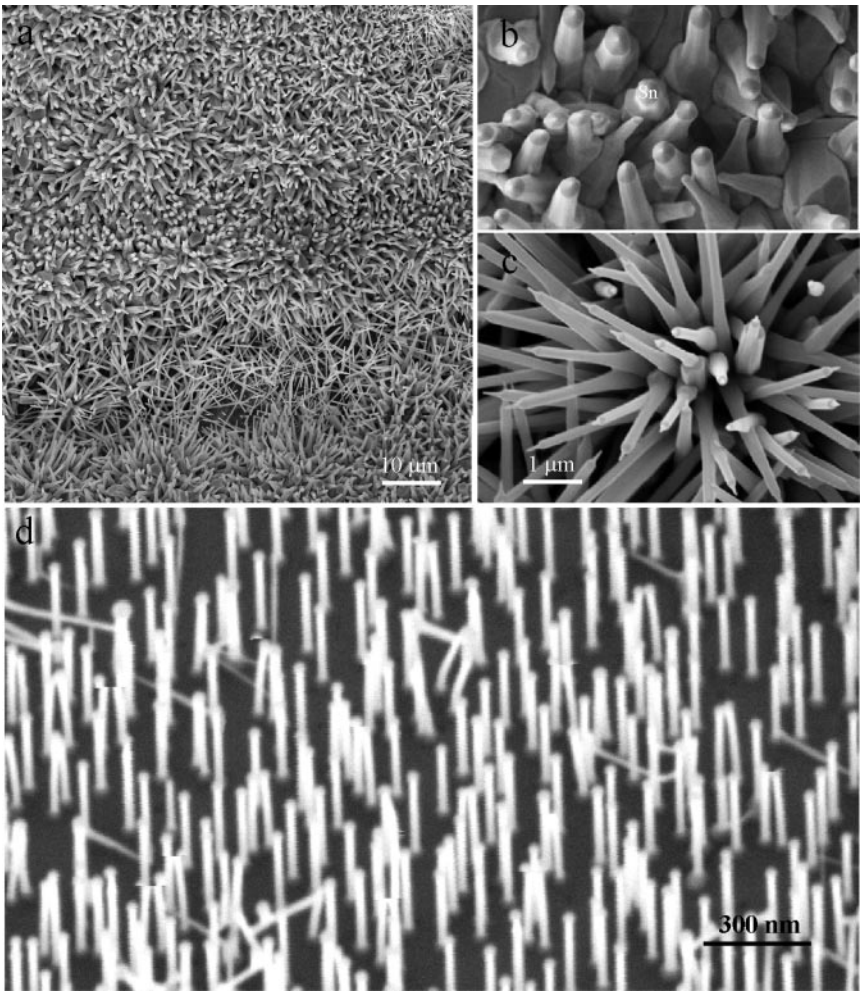

Figure 11 (*a*,*b*,*c*) Low-magnification and high-magnification SEM images of ZnO nanorods grown on alumina substrate with Sn at the growth front. (*d*) Orientation-ordered epitaxial growth of ZnO nanorods on a large ZnO crystal, showing identical orientation.

GROWTH MECHANISM

Anisotropic Growth Via Vapor-Liquid-Solid Processes

Understanding the growth mechanism is critical in controlling and designing nanostructures. In the 1950s and 1960s or even earlier, it had been found in a study of whisker growth that acicular-structured oxides of metals such as Cu, Cr,

Fe, Pb, Ti, W, and Zn could be produced on the external surfaces of corresponding metals when heated in air at certain temperatures (53). Formation of the acicular oxides can be regarded as vapor-solid growth. Frank's dislocation growth mechanism (54) had been widely accepted for the growth of crystal whiskers, in which a screw dislocation with its Burgers' vector parallel to the growth direction provides self-perpetuating growth steps on the tip so that the tip is an efficient sink for adsorbing atoms.

Later, in the early 1960s, another crystal growth mechanism of the vapor-liquid-solid (VLS) process was proposed by Wagner and Ellis (55) in their investigation of Si whisker growth. According to the VLS growth mechanism, the anisotropic crystal growth is guided by a droplet of liquid alloy. The droplet surface has a relatively higher sticking coefficient and is therefore a preferred adsorption site for arriving vapor reactant. As the liquid droplet becomes supersaturated with the vapor reactant, whisker growth will occur by means of a precipitation process of the reactant. The role of the droplet in the crystal growth process is analogous to a catalyst in a chemical reaction; VLS growth is also called catalysis growth. The whiskers grown by VLS were usually on the micrometer scale in their diameter. On the basis of the VLS growth mechanisms, a series of wire-like nanostructures have been synthesized for element semiconductors (9), compound semiconductors (56), and oxides such as ZnO (51), SiO_2 (57), Ga_2O_3 (58, 59), and In_2O_3 (60). Analogous to the VLS growth, a solution-liquid-solid growth method was also developed recently to grow semiconductor nanowhiskers and nanowires at low temperature (61).

Oxide-assisted growth is another mechanism proposed for nanowire formation in vapor growth (62). Under low-temperature conditions, decomposition of the unstable oxide provides the nucleus for nanowire formation, and the temperature gradient provides the driving force for nanowire growth.

Kinetics of Anisotropic Growth Via Vapor-Solid Processes

Recently, a variety of wire-like nanostructures of oxides including nanowires (63), nanorods (64), and nanobelts (19, 32) have been produced by vapor growth methods without introducing any hetero-metal catalyst. The growth was likely governed by the vapor-solid process (19). Usually, the crystalline wire-like nanostructures are not cylindrical wires but have a faceted shape that consists of certain low-index crystallographic planes. It seems that surface energy minimizing may play an important role in the formation of nanobelts and nanowires. The surface energy minimizing is, however, not sufficient, at least for interpreting the formation of In_2O_3 and CdO nanobelts, both of which have cubic lattice structures and are enclosed by $\pm(100)$, $\pm(010)$, and $\pm(001)$ crystal planes that are crystallographically equivalent. It may be argued that surface energy plays a key role in the formation of the nanobelt structure, but it has been found that amorphous silica can also form nanowire structures (12, 65, 66). These findings therefore imply that the formation of wire-like nanostructures may be controlled by kinetics during crystal growth.

Temperature and the supersaturation ratio are two dominant processing factors in controlling the morphology of the product in vapor-solid growth processes. Much work has been done both experimentally and theoretically on the kinetics of whisker growth (67–69).

VAPOR-SOLID-PROCESS GROWTH OF OXIDE NANOBELTS

To understand the growth of a uniform belt structure without the presence of hetero-catalysis particles, we propose a possible mechanism that may present in nanobelt growth (33). The source material is assumed to vaporize into molecular species at high temperature, and the molecules are composed of the stoichiometric cation-anion molecules (Figure 12*a*). When condensed onto the substrate at a lower temperature region, the cation-anion molecules will be arranged in such a way that a proper cation-anion coordination is preserved to balance the local charge

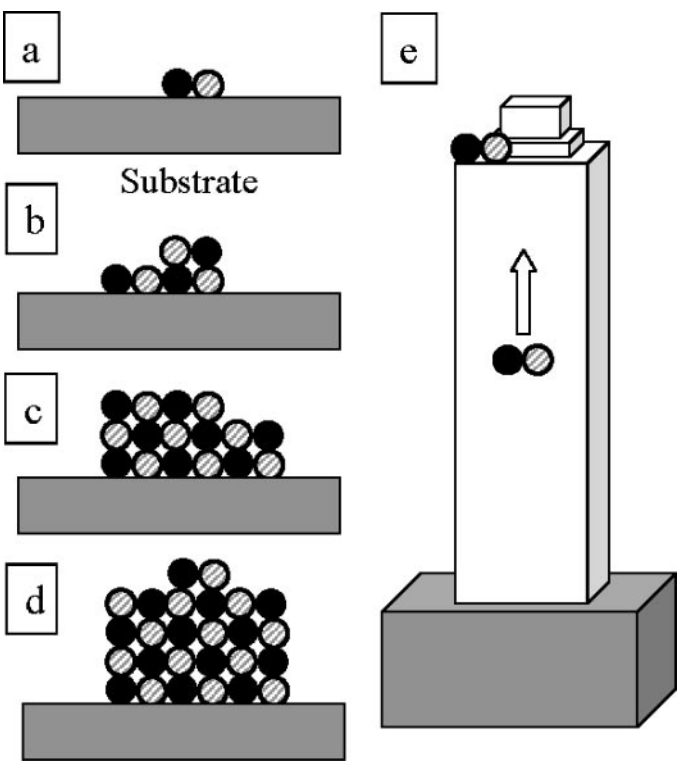

Figure 12 A proposed growth process of a nanobelt (see text for details).

and structural symmetry (Figure 12*b*), forming a small nucleus. The newly arrived molecules will continue to deposit on the formed nucleus, while the surfaces that have lower energy, such as the side surfaces, start to form. Because the growth temperature is in the range of 800–1000°C, the mobility of the atoms and molecules is high enough, and the low-energy surface tends to be flat, thus preventing the accumulation of the newly arrived molecules onto the surface, resulting in expansion in surface area as more molecules stick on the rough growth front (Figure 12*c*). The rough structure of the tip leads to a rapid accumulation of incoming molecules, resulting in the fast formation of a nanobelt (Figure 12*d*), and after some time a nanobelt is formed (Figure 12*e*). The newly arrived molecules can continue to stick on the growth front, or the side surfaces, but the smooth side surface and the high molecular mobility at the growth temperature prevents them from remaining on the surface. The molecules randomly diffuse on the surface and finally find the lower-energy sites at the growth front. The molecules are unlikely to stick to the edge of the nanobelts because of the unbalanced coordination and possibly higher energy. The size of the nanobelt cross section is determined by the growth temperature and supersaturation ratio in kinetics of crystal growth, as mentioned above.

SELF-CATALYZED GROWTH

Self-catalyzed growth could be an important process in the formation of nanobelts, in which a small thin layer or even an atom-thickness metal layer such as Zn presents at the growth front, which could lead to growth (70). The layer could be quickly oxidized after the nanobelts are exposed to air after growth, but our ex-situ analysis never found this layer. Our recent study of ZnO nanobelts has shed some light on self-catalysis.

Figure 13*a* shows a $[01\bar{1}0]$ high-resolution TEM profile image recorded from the growth front of a nanobelt growing along [0001]. The side and front surfaces are rough, and there are tiny nanocrystals being formed at the growth front. These nanocrystals preserve the orientation of the nanofingers and possibly grow epitaxially, and their lattice spacing fits to ZnO, as presented in the enlarged image from the growth front (Figure 13*b*). The top layer of the nanocrystal has a darker contrast, possibly indicating an enrichment of Zn at the local region. A striking feature observed in the image is the presence of some dark spots at the growth front, indicated by an arrowhead. These tiny clusters of sizes $\sim$0.5 nm may correspond to tiny Zn clusters.

NANOTECHNOLOGY BASED ON NANOBELTS

Semiconducting transition and rare-earth metal oxides are attracting significant attention as candidates for chemical and environmental sensors (71–74). This is because their electrical conductivity is highly dependent on the nature and

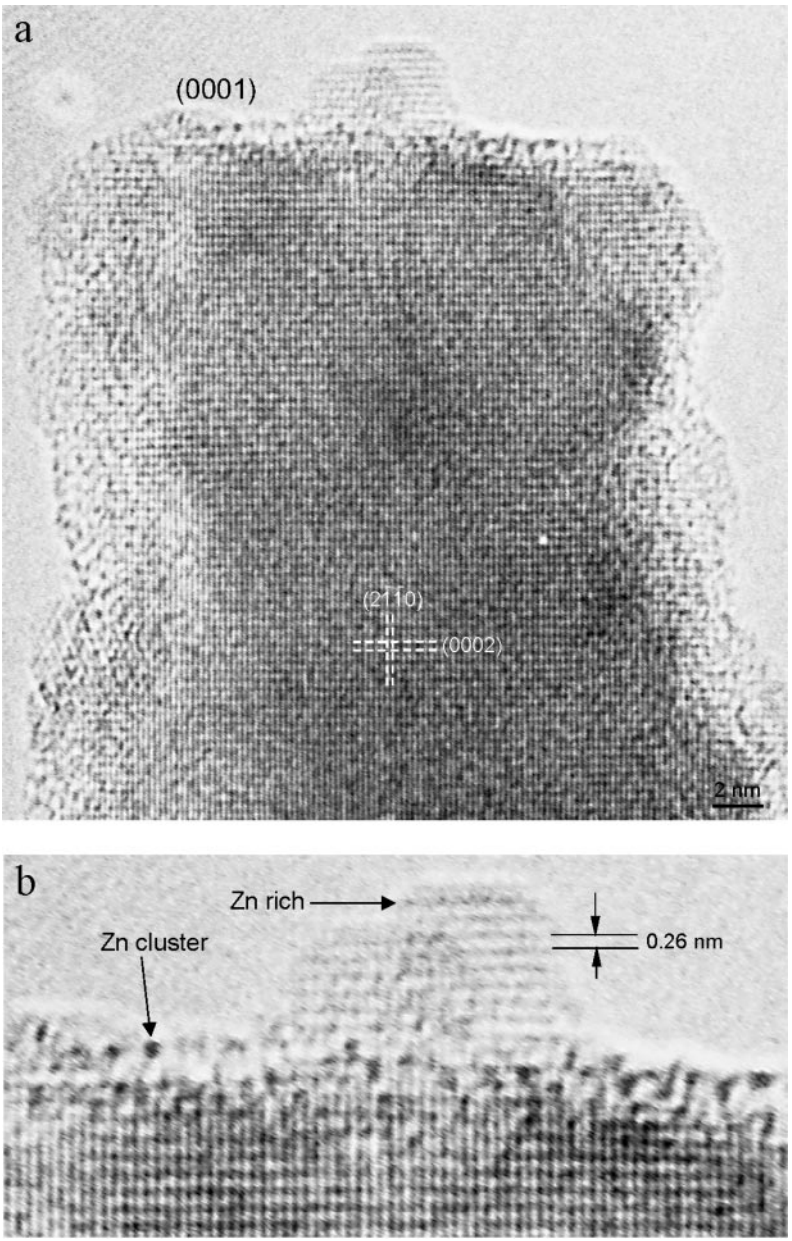

Figure 13 (*a*) High-resolution TEM image recorded from a nanofinger growing along [0001], showing rougher surface and the presence of small ZnO nanocrystals as well as possible Zn clusters at the growth front. (*b*) An enlargement of the growth front to display the fine structures. The image suggests the presence of Zn clusters at the growth front, which may self-catalyze the process for the growth.

concentration of the surfaces of adsorbed species. The key characteristics of these oxides are (*a*) cations with mixed valence and (*b*) oxygen vacancies. The latter are responsible for the observed high sensitivity of the electrical properties to the presence of adsorbed molecules and allow the tuning of the conductance of the oxide. The semiconducting oxide nanobelts grown by our group are structurally perfect and geometrically uniform. These nanostructures are ideal materials for building nano-sized devices and sensors.

FIELD-EFFECT TRANSISTOR BASED ON A SINGLE NANOBELT

Field-effect transistors have been fabricated using individual nanobelts (75). Large bundles of either SnO_2 or ZnO nanobelts were dispersed in ethanol by ultrasonication until mostly individual nanobelts were isolated. These ethanol dispersions were dried onto a SiO_2/Si substrate for imaging by noncontact-mode atomic force microscopy. SnO_2 field-effect transistors were fabricated by depositing SnO_2 nanobelt dispersions onto SiO_2/Si (p^+) substrates, followed by treatment in an oxygen atmosphere at 800°C for 2 h. The SiO_2/Si substrates were then spin-coated with poly(methyl methacrylate) (PMMA), baked, exposed to electron-beam lithography for the definition of electrode arrays, and developed. A 30-nm-thick layer of titanium was deposited by electron-beam evaporation to serve as the source and drain electrodes, and the remaining PMMA was lifted off in hot acetone. An atomic force microscopy image of the field-effect transistor (FET) and the schematic diagram are given in Figure 14*a*. The principle of this device is that controlling the gate voltage controls the current flowing from the source to the drain.

An alternative way of contacting the nanostructures was applied to ZnO nanobelts. In this case FETs were fabricated by depositing dispersed ZnO nanobelts on predefined gold electrode arrays. In both cases the SiO_2 gate dielectric thickness was 120 nm, and the back gate electrode was fabricated by evaporation of gold on the Si (p^+) side of the substrate. Also, in both fabrication schemes, the electrode arrays were variably spaced. They included electrode gaps as small as 100 nm and as large as 6 μm.

By forming metal electrode–nanostructure electrical contacts and capacitive coupling the nanostructure to a nearby gate electrode, an FET is produced using a nanobelt that allows the exploration of new aspects of the physical and chemical properties of the nanostructures (76–78).

The alternative way of contacting the nanobelts by simply depositing them on top of prefabricated gold electrodes led to very resistive contacts. A typical ZnO FET showed a gate threshold voltage of -15 V, a switching ratio of nearly 100, and a peak conductivity of 1.25×10^{-3} $(\Omega\text{-cm})^{-1}$. A completely analogous behavior has been observed in the case of carbon nanotubes deposited on top of Au electrodes or covered by Ti electrodes (79).

TUNABLE ELECTRICAL PROPERTIES OF NANOBELTS

The conductivity of a nanobelt can be tuned by controlling its surface and volume oxygen deficiency (75). Before electrical measurement, SnO_2 nanobelts are annealed in a 1-atm oxygen environment at 800°C for 2 h. Without this treatment, the as-produced nanobelts exhibit no measurable conductivity for source-drain biases from −10 V to 10 V and for gate biases from −20 V to 20 V, while after this treatment the SnO_2 nanobelts exhibit considerable conductivity. By further annealing of the devices at lower temperatures in vacuum, oxygen, or ambient, the electrical properties of the nanobelts can be tuned.

After annealing of the SnO_2 devices in vacuum at 200°C, the nanobelt conductivity increases along with an associated negative-shift in gate-threshold voltage. Smaller, additional increases in conductivity are observed after additional vacuum anneals. Eventually, the nanobelt behaves like a metal, with the gate field being unable to affect the current flowing through the device. In contrast, annealing nanobelt devices in ambient at 200°C leads to a decrease of the conductivity, along with a shift in the gate-threshold voltage in the opposite, positive direction (Figure 14*b*). The source-drain conductivity at zero gate bias spans 3 orders of magnitude from 0.09 $(\Omega\text{-cm})^{-1}$ after annealing at 200°C in ambient to 75.3 $(\Omega\text{-cm})^{-1}$ after annealing at 250°C in vacuum. The changes in conductivity with low-temperature annealing most likely result from variations in the number of oxygen species adsorbed on the SnO_2 surfaces or in the number of oxygen vacancies in the SnO_2 bulk with the amount of oxygen in the environment (80). The number of equilibrium surface and bulk oxygen defects are a function of the environmental oxygen partial pressure and temperature. Annealing in vacuum should decrease the number of adsorbed oxygen species and increase the number of bulk oxygen vacancies, while annealing in oxygen or ambient should do the opposite. It is well established that bulk and surface oxygen vacancies in SnO_2 act as electron donors, which should increase SnO_2 conductivity and decrease the gate-threshold voltage (81). This is precisely what we have observed.

It should be noted that the SnO_2 nanobelt conductivity increases and the gate-threshold voltage decreases simply by taking a nanobelt device from ambient into vacuum without annealing (Figure 14*b*). Since the diffusion of bulk oxygen vacancies at room temperature are limited (82, 83), this indicates that surface oxygen desorption most likely takes place at this temperature. Because of their small dimensions, semiconducting oxide nanobelts have on the order of 10^{20} surface oxygen sites per cubic centimeter of material (84). Thus, even for partial changes in the concentration of adsorbed oxygen species, large changes in nanobelt conductivity can be observed.

As noted, annealing at 200°C and 250°C induces further changes in conductivity (Figure 14*b*). To account for this, either the surface or bulk nanobelt composition must change as a result of these annealing steps. Mizusaki et al. (84) have argued that for temperatures below 900°C, the equilibrium bulk nonstoichiometry of SnO_2 will be insignificant in comparison to surface nonstoichiometry in

samples of similar surface-to-volume ratios. This suggests that surface oxygen vacancies should control conductivity after 200°C and 250°C anneals. Annealing might also desorb species other than oxygen from the nanobelt surfaces. Water could act as a mask on the nanobelt surface, decreasing sensitivity to environmental oxygen until removed. The strong dependence of the conductance on the oxygen deficiency in nanobelts is an important characteristic of functional oxide, which is capable of tuning and controlling the electrical properties of the nanodevice.

PHOTOCONDUCTIVITY OF NANOBELTS

UV–light irradiation of the nanobelt diode of SnO_2 in air results in a significant increase of the conductivity (Figure 15). Light with a wavelength of 350 nm ($E_\lambda = 3.54$ eV) was used, exceeding the direct band-gap of SnO_2. The increase in the conductivity results from photogeneration of electron-hole pairs as well as doping by UV light–induced surface desorption (85–87). These processes could be observed by introducing a shutter between the light source and the SnO_2 nanobelt so that the flux of UV photons could be turned on and off.

The unique geometrical shape of nanobelts is ideal for field emission. MoO_3 nanobelts have been shown to exhibit superior performance (27, 26). The work function at the tips of individual ZnO nanobelts has been measured by a novel technique (88).

GAS SENSORS BASED ON NANOBELTS

Conductometric metal oxide semiconductor thin films are the most promising devices among solid state chemical sensors, due to their small dimension, low cost, low power consumption, on-line operation, and high compatibility with microelectronic processing. The fundamental sensing mechanism of metal oxide–based gas sensors relies on a change in electrical conductivity due to the interaction process between the surface complexes, such as O^-, O_2^-, H^+, and OH^-, reactive chemical species and the gas molecules to be detected.

Although many oxides have been investigated for their gas-sensing properties, commercially available gas sensors are mainly made of SnO_2 in the form of thick films, porous pellets, or thin films. The effects of the microstructure, namely, ratio of surface area to volume, grain size, and pore size of the metal oxide particles, as well as film thickness of the sensor are well recognized. Lack of long-term stability has until recently prevented a wide range application of this type of sensor. Nanobelts of semiconducting oxide, with a rectangular cross section in a ribbon-like morphology, are very promising for sensors because their surface-to-volume ratio is very high, the oxide is single crystalline, the faces exposed to the gaseous environment are always the same, and the size is likely to produce

a complete depletion of carriers inside the belt (89). In addition, the deposition technique is very simple and cheap and the size and shape can be easily controlled. In polycrystalline and thick-film devices, only a small fraction of the species adsorbed near the grain boundaries is active in modifying the device electrical-transport properties.

In the new sensors based on single-crystalline nanobelts, almost all of the adsorbed species are active in producing a surface depletion layer. Free carriers should cross the belts' volume along the axis in a FET channel–like way. In addition, because the size of the depletion layer for tin oxide, due to oxygen desorption, penetrates 50 nm or more through the bulk, the belts are probably almost as depleted of carriers as a pinched-off FET because the belt thickness is typically less than 50 nm. The presence of poisoning species should switch the structures from pinched-off to conductive channel, strongly modifying the electrical properties. A further reduction of belt size could bring the development of quantum-confined structures and nanodevices.

For the fabrication of sensors, a platinum interdigitative electrode structure was made using a lithography and metal-deposition technique on an alumina substrate. A platinum heater was attached to the back of the substrate to control the working temperature of the sensor. Then, several nanobelts were placed onto the electrodes for measuring their electric conductance, and a proper measure was taken to ensure the contact of the nanobelts with the electrodes. The flow-through technique is used to determine the gas-sensing properties of the thin films. A constant flux of synthetic air equal to 0.3 liters/min, mixed with the desired amount of gaseous species, flows through a stabilized sealed chamber at 20°C, atmospheric pressure and controlled humidity. Electrical characterization was carried out by a volt-amperometric technique at constant bias of 1 V, and a picoammeter measured the change of electrical current.

Figure 16 reports the isothermal response of the current flowing through the tin oxide nanobelts as two square concentration pulses of CO (250 and 500 ppm, respectively) being fed into the test chamber at a working temperature of 400°C and 30% RH (relative humidity at 20°C). The electric current increases for about 60% and 100% with the introduction of 200 and 500 ppm CO, respectively. The sensor response, defined as the relative variation in conductance due to the introduction of gas, is about $\Delta G/G = 0.9$.

Figure 16*a* also shows the isothermal response of the current flowing through the nanobelts as a square concentration pulse of 0.5 ppm nitrogen dioxide is fed into the test chamber at a working temperature of 400°C and 30% RH. The sensor response is $\Delta G/G = -15.5 = -1550\%$, which is extremely high and sensitive. This means that the sensitivity of the sensor is on the level of a few parts per billion.

In general, the selectivity of the oxide is a concern. This may be improved by fabricating sensors using several types of nanobelts, or by functionalizing the surfaces of the nanobelts. It is, however, very important to note that CO and ethanol increase the conductivity, while NO_2 decreases the conductivity of the SnO_2 nanobelts.

The small size offered by the sensors based on individual nanobelts is a major advantage for application in biotechnology, because it gives the potential of implanting in biological systems. Nanosensors based on nanobelts may be unique in detecting single cancer cells and measuring pressure in biofluid.

HEAT TRANSPORT THROUGH A NANOBELT

Heat transport at nanoscale is very interesting and technologically important. With the reduction of object size, phonon modes and phonon density of states change drastically, resulting in unusual thermal transport phenomena in mesoscopic systems. Theoretical investigation of thermal conductance in a one-dimensional nanowire predicted quantum effects at very low temperature: $G_{th} = \pi^2 K_B^2 T/3h$ (90). Experimental measurement has proved this prediction (91). Thermal transport along a single SnO_2 nanobelt has also been carried out (Figure 17*a*) (92). Thermal contact micropads have been fabricated using a lithography technique. The thermal conductance across the nanobelt measured as a function of the local temperature is given in Figure 17*b*. The thermal conductivity of the nanobelts is significantly suppressed in comparison to bulk, owing to increased phonon-boundary scattering and modified phonon dispersion (93). This size effect can lead to localized heating in nanoelectronics (94) but may find potential use for improving thermoelectric performance.

NANOBELTS AS NANORESONATORS

Another key quantity in the application of nanobelts is their bending modulus. We have measured this quantity using a technique developed for carbon nanotubes. Based on the electric field–induced resonant excitation, the mechanical properties of individual nanowire-like structures can be measured by in situ TEM (95, 96). Using this method, mechanical properties of carbon nanotubes (95, 97), silicon nanowires (18), and silicon carbide–silica composite nanowires (18) have been quantified.

To carry out the mechanical property measurements of a nanobelt, a specimen holder for a Hitachi HF-2000 TEM (200 kV) was built for applying a voltage across a nanobelt and its counter electrode. Mechanical resonance can be induced if the applied frequency matches the natural resonance frequency of the nanobelt. Due to the mirror symmetry of the nanobelt, there are two distinct fundamental resonance frequencies corresponding to the vibration in the thickness and width directions, which are given from the classical elasticity theory as (98)

$$\nu_x = \frac{\beta_1^2 T}{4\pi L^2}\sqrt{\frac{E_x}{3\rho}}, \qquad (4)$$

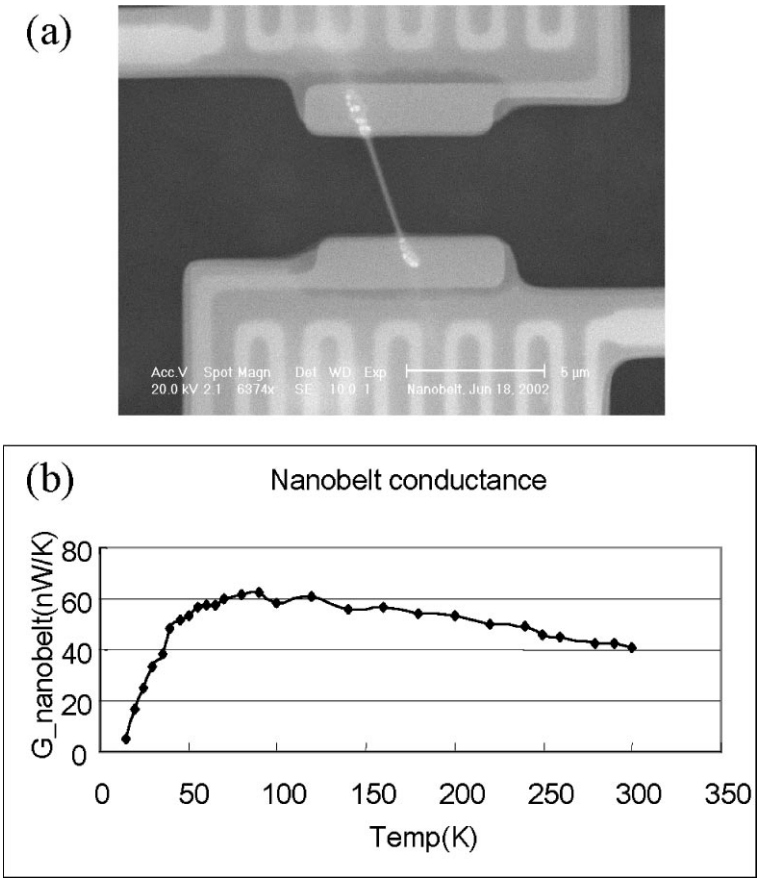

Figure 17 Measurement of thermal transport through a single SnO_2 nanobelt.

$$\nu_x = \frac{\beta_1^2 W}{4\pi L^2}\sqrt{\frac{E_y}{3\rho}}, \tag{5}$$

where $\beta_1 = 1.875$ for the first harmonic resonance; E_x and E_y are the bending modulus if the vibration is along the x-axis (thickness direction) and y-direction (width direction), respectively; ρ is the density, L is the length, W is the width, and T is the thickness of the nanobelt. The two modes are decoupled and they can be observed separately in experiments.

Changing the frequency of the applied voltage, we found two fundamental frequencies in two orthogonal directions transverse to the nanobelt (99). Figure 18*a,b* shows the harmonic resonance, with the vibration planes nearly perpendicular and parallel to the viewing direction, respectively. For calculating the bending modulus, it is critical to accurately measure the fundamental resonance frequency (υ_1)

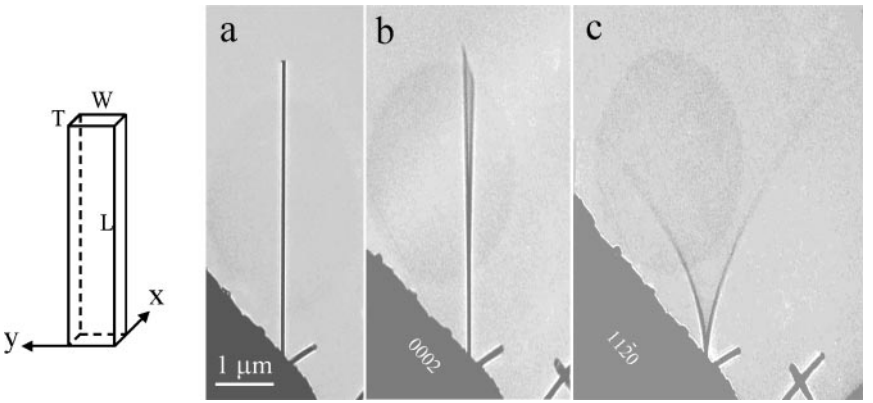

Figure 18 Nanoresonators made of nanobelts. Measuring the bending modulus of a ZnO nanobelt by electric field–induced mechanical resonance in TEM. (*a*) Geometrical shape of a nanobelt. (*b*,*c*) Mechanical resonance of a nanobelt along the two orthogonal directions closely perpendicular to the viewing direction ($\nu_x = 622$ KHz) and nearly parallel to the viewing direction ($\nu_y = 691$ KHz), respectively.

and the dimensional sizes (L and T or W) of the investigated ZnO nanobelts. To determine ν_1, we have checked the stability of resonance frequency to ensure that one end of the nanobelt is tightly fixed and the resonant excitation has been carefully checked around the half value of the resonance frequency. The specimen holder can be rotated about its axis so that the nanobelt can be aligned perpendicular to the electron beam so the real length (L) of the nanobelt can be measured. The projection direction along the beam is determined by the electron diffraction pattern, so that the true thickness and width can be determined because the normal direction of the nanobelt is [$\bar{2}$110]. Based on the experimental data, the bending moduli of ZnO nanobelts can be calculated using Equation 1 or 2. The experimental results are summarized in Table 2 (99). The bending modulus of the ZnO nanobelts was ~52 GPa. Our experiments clearly show that nanobelts

TABLE 2 Bending modulus of the ZnO nanobelts (E_x and E_y represent the bending modulus corresponding to the resonance along the thickness and width directions, respectively)

	Length L (μm)	**Width W (nm)**	**Thickness T (nm)**	**Fundamental Fequency (kHz)**				**Bending Modulus (GPa)**	
Nanobelt	(±0.05)	(±1)	(±1)	W/T	ν_{x1}	ν_{g1}	ν_{g1}/ν_{x1}	E_x	E_y
1	8.25	55	33	1.7	232	373	1.6	46.6 ± 0.6	50.1 ± 0.6
2	4.73	28	19	1.5	396	576	1.4	44.3 ± 1.3	45.5 ± 2.9
3	4.07	31	20	1.6	662	958	1.4	56.3 ± 0.9	64.6 ± 2.3
4	8.90	44	39	1.1	210	231	1.1	37.9 ± 0.6	39.9 ± 1.2

can be effective nanoresonators exhibiting two orthogonal resonance modes, which can be used as probes for scanning probe microscopy (SPM) operated in tapping and scanning modes.

Using a technique developed for measuring the work function at the tip of a carbon nanotube (100), the work function at the tip of an oxide nanobelt has also been measured (101).

NANOBELTS AS NANOCANTILEVERS

Cantilever-based SPM techniques are one of the most powerful approaches in imaging, manipulating, and measuring nanoscale properties and phenomena. The most conventional cantilever used for SPM is based on silicon, Si_3N_4 or SiC, which is fabricated by an e-beam or optical lithography technique and has typical dimensions of thickness ~100 nm, width ~5 μm, and length ~50 μm. Utilization of nanowire- and nanotube-based cantilevers can have several advantages for SPM. Carbon nanotubes can be grown on the tip of a conventional cantilever and be used for imaging surfaces with a large degree of abrupt variation in surface morphology (102). We have demonstrated the manipulation of nanobelts by atomic force microscopy and their potential for use as nanocantilevers (103).

Combining microelectromechanical system technology with self-assembled nanobelts, we were able to produce cost-effective cantilevers with much improved sensitivity for a range of devices and applications. Force, pressure, mass, thermal, biological, and chemical sensors are all prospective devices. Semiconducting nanobelts are ideal candidates for cantilever applications. Structurally they are defect-free single crystals, providing excellent mechanical properties. The reduced dimensions of nanobelt cantilevers offer a significant increase in cantilever sensitivity. Combining the aforementioned techniques with micromanipulation has led to the horizontal alignment of individual ZnO nanobelts onto silicon chips. The aligned ZnO cantilevers shown in Figure 19 were manipulated to have a range of lengths. This exemplifies our ability to tune the resonance frequency of each cantilever and thus modify cantilevers for different applications such as contact, noncontact, and tapping mode atomic force microscopy. Periodic contrast of the ZnO cantilevers is observed as a result of electronic charge–induced vibrations during SEM operation. Such contrast is absent in regions where the nanobelts are in direct contact with the silicon substrate, suggesting adequate adhesion forces between the cantilevers and the silicon chip.

PIEZOELECTRIC NANOBELTS WITH POLAR SURFACE

The noncentral symmetry and the tetrahedral coordinated $(ZnO_4)^{6-}$ unit in ZnO result in anisotropic piezoelectric properties. Structurally, the Wurtzite-structured ZnO crystal is described schematically as a number of alternating planes composed of fourfold coordinated O^{2-} and Zn^{2+} ions, stacked alternately along the c-axis.

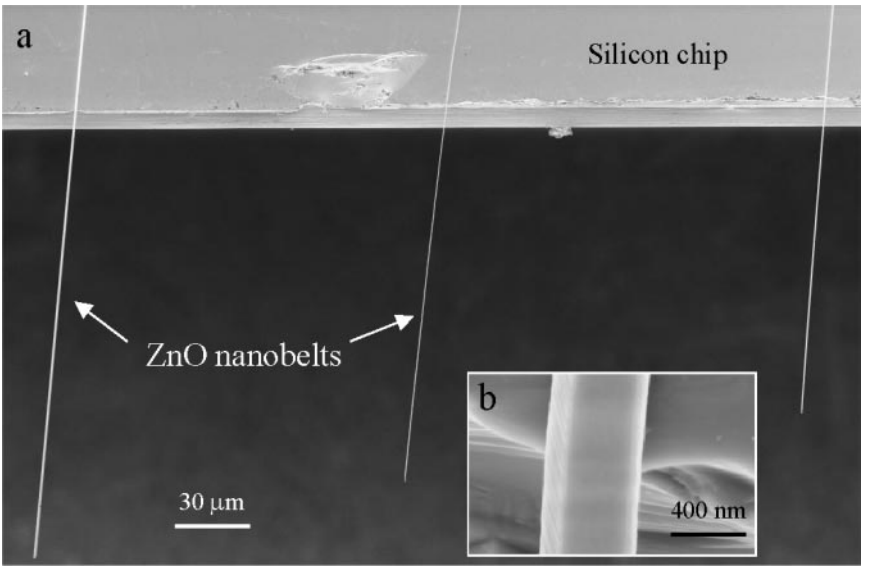

Figure 19 (*a*) Nanobelts as ultrasmall nanocantilever arrays aligned on a silicon chip. (*b*) An enlarged SEM image recorded from the nanobelt cantilever.

The oppositely charged ions produce positively charged (0001)-Zn and negatively charged (0001)-O polar surfaces, resulting in a normal dipole moment and spontaneous polarization as well as a divergence in surface energy. To maintain a stable structure, the polar surfaces generally have facets or exhibit massive surface reconstructions, but ZnO $\pm(0001)$ is an exception, which is atomically flat, stable, and without reconstruction (104, 105). Understanding the superior stability of the ZnO $\pm(0001)$ polar surfaces is a forefront research topic in today's surface physics (106–109).

ZnO has a rich family of structures, which are mainly defined by the $(000\bar{1})$, $\{01\bar{1}0\}$, and $\{2\bar{1}\bar{1}0\}$ facets as well as the anisotropic growth along [0001], $\langle 01\bar{1}0\rangle$, and $\langle 2\bar{1}\bar{1}0\rangle$. The most desirable morphology to maximize the piezoelectric effect is to create nanostructures that preserve large (0001) polar surfaces (110, 111). However, ZnO (0001) has a surface energy that diverges with sample size due to the surface polarization charge. Therefore, growth of (0001) surface-dominated freestanding nanostructures needs to overcome the barrier of surface energy.

We have recently successfully synthesized ZnO nanobelts that are dominated by the (0001) polar surface (112). Hundreds of nanobelts laid down naturally onto a carbon film by electron diffraction were examined. More than 90% of them showed the same orientation of [0001] with respect to the incident electron beam (Figure 20*a*), indicating that the top flat surfaces of the nanobelts are the polar $\pm(0001)$ facets. This clearly demonstrates the success of overcoming the surface energy barrier by growth kinetics in achieving structural control. The ZnO nanobelt has a Wurtzite structure with lattice constants of $a = 0.325$ nm and

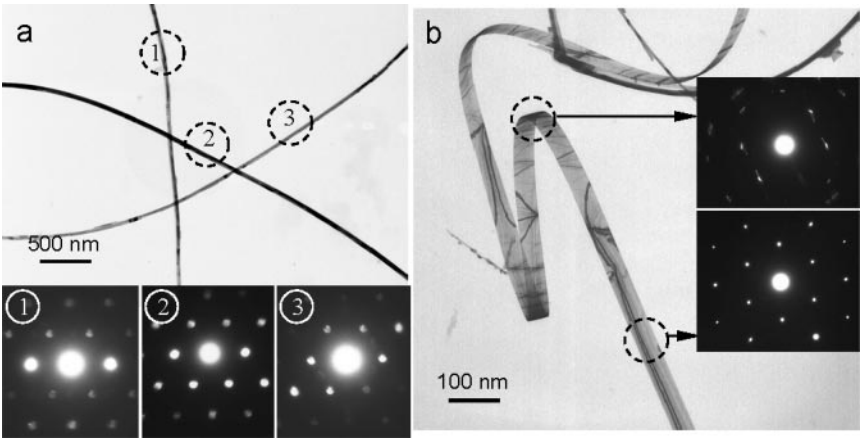

Figure 20 Controlled growth of (0001) polar surface–dominated ZnO nanobelts. (*a*) Low-magnification TEM images and the corresponding electron diffraction patterns recorded from the areas as indicated by a sequence number from a TEM grid without tilting, showing their unanimous [0001] orientation on a flat carbon substrate. (*b*) Low-magnification TEM image and the corresponding electron diffraction patterns recorded from the circled regions, displaying the geometry of the nanobelt. The difference between the two electron diffraction patterns is due to the bending in the local regions. The contrast observed in the image is the bending contour in electron imaging produced by the deformation of atomic planes.

$c = 0.521$ nm. Indexing of the electron diffraction pattern shows that the nanobelt grows along $[2\bar{1}\bar{1}0]$ (the *a*-axis), with its top and bottom surfaces $\pm(0001)$ and the side surfaces $\pm(01\bar{1}0)$. High-resolution TEM shows that the nanobelt is single crystalline without the presence of dislocations. Due to the small thickness of 5–20 nm and large aspect ratio of ∼1:4, the flexibility and toughness of the nanobelts are extremely high, so they can be bent or twisted without fracture (Figure 20*b*).

Nanobelts with large polar surfaces are ideal systems for understanding piezoelectricity and polarization-induced ferroelectricity at nano-scale. The different polar surfaces can be used as selective catalysts. The piezoelectric and ferroelectric nanobelt structures could be nano-scale sensors, transducers, and resonators, which are functional components for a microelectromechanical system and nanoelectromechanical system.

NANORINGS AND NANOHELIXES OF PIEZOELECTRIC NANOBELTS

A striking new phenomenon for the piezoelectric nanobelt presented in Figure 20 is the formation of helical structures by rolling up single-crystalline nanobelts (Figure 21*a–c*) (112). This is the first report that a single crystal nanobelt can

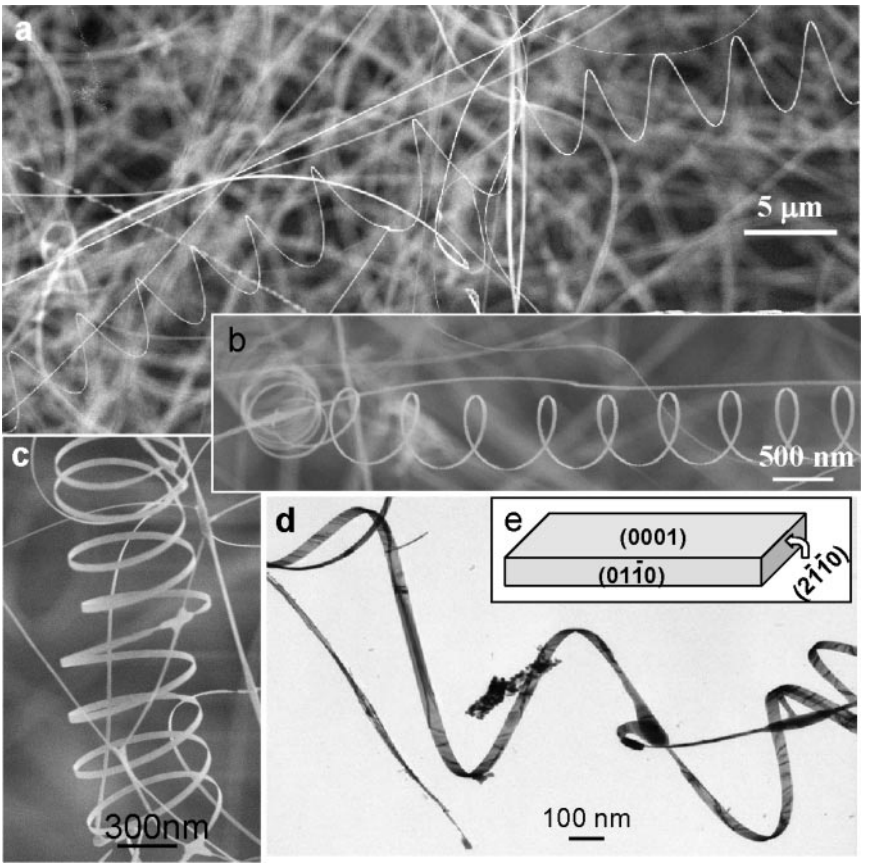

Figure 21 Nanosprings and nanorings of piezoelectric nanobelts. (*a–c*) SEM images of the as-synthesized single-crystal ZnO nanobelts, showing helical nanosprings. The typical width of the nanobelt is ∼30 nm, and pitch distance is rather uniform. (*d*) TEM image of a helical nanospring made of a single-crystal ZnO nanobelt. (*e*) The structure model of the ZnO nanobelt.

form helical nanosprings and nanorings. The helical nanostructure has a uniform shape, with radii of ∼500–800 nm and evenly distributed pitches. Each is made of a single-crystal ZnO nanobelt that is dominated by the (0001) polar surface. Electron diffraction indicates that the direction of the radius toward the center of the helical ring is always [0001] along the entire perimeter without significant twisting, and the circular plane of the nanoring is [01$\bar{1}$0]. A TEM image of a helical nanospring is presented in Figure 21*d*, showing the projected shape of the single-crystal twisted nanobelts. A model of the structure of the nanobelt is shown in Figure 21*e*. These types of helical nanosprings and nanorings are observed only for the (0001) plane-dominated ZnO.

The formation of the nanorings and nanohelicals can be understood from the nature of the polar surfaces. The (0001) plane can be terminated with Zn [(0001)-Zn] or oxygen [(000$\bar{1}$)-O], resulting in positively and negatively charged top and bottom surfaces, respectively. Physically, if the surface charges are uncompensated during growth, the net dipole moment tends to diverge and the electrostatic energy increases. For a thin nanobelt lying on a substrate, the spontaneous polarization induces electrostatic energy due to the dipole moment, but rolling up to form a circular ring would minimize or neutralize the overall dipole moment, reducing the electrostatic energy. However, bending of the nanobelt produces elastic energy. The stable shape of the nanobelt is determined by the minimization of the total energy contributed by spontaneous polarization and elasticity. A model calculation agrees very well with the physical picture we have described (112).

The growth of polar facet–dominated nanobelt surfaces is a major step toward development of piezoelectric one-dimensional nanostructures. Since the ZnO ($2\bar{1}\bar{1}0$) plane has a surface energy lower than that of either (0001) or ($01\bar{1}0$), a fast growth along [$2\bar{1}\bar{1}0$] (a-axis) to form a nanobelt structure may be unfavorable from the energy point of view. However, the success of controlled growth of free-standing (0001) polar surface–dominated nanobelts along the a-axis demonstrates the experimental feasibility of overcoming the energy barrier through growth kinetics, thus providing a feasible approach for growing structurally controlled nanobelts of technological importance.

Helical structure is the most fundamental structural configuration for DNA and many biological proteins and is due to van der Waals force and hydrogen bonding. For one-dimensional nanostructures, nanocoils and nanorings have been observed for carbon nanotubes (113–115) and SiC (116). The former are created by a periodic arrangement of the paired pentagon and heptagon carbon rings in the hexagonal carbon network (117), and the latter by a stacking of platelets around the growth axis (118). These helical structures are produced by the presence of point or planar defects (twins and stacking faults), which is a completely different mechanism from the process that we have proposed for the formation of single-crystal helical nanosprings and nanorings. The striking new feature of the helical nanostructures for single-crystalline ZnO nanobelts is that they are spontaneous polarization–induced structures. The nanobelts and helical nanostructures are an ideal system for understanding piezoelectricity and polarization-induced ferroelectricity at nanoscale. The different polar surfaces could be used as selective catalysts. The piezoelectric and ferroelectric nanobelt structures could be nanoscale sensors, transducers, and resonators.

POLAR SURFACE–INDUCED ASYMMETRIC GROWTH

Comb structures of ZnO have been reported (119), but the mechanism that drives the growth was not elaborated. The comb structures we have received recently (Figure 22) with the comb-teeth grow along [0001], the top and bottom surfaces

Figure 22 SEM image of comb-like nanostructure of ZnO, which is the result of surface polarization–induced growth.

being $\pm(01\bar{1}0)$ and the side surfaces $\pm(\bar{2}110)$. As presented above, the ZnO (0001) surface can be terminated with Zn or O. Using advanced TEM and a convergent-beam electron-diffraction technique, we found that the comb structure is due to the surface polarity (70). The positively charged ZnO (0001)-Zn surface is chemically active, and the negatively charged $(000\bar{1})$-O surface is inert in the growth of nanocantilever arrays. Longer and wider nanofinger arrays are grown from the (0001)-Zn surface, which is suggested to be a self-catalyzed process due to the enrichment of Zn at the growth front. The chemically inactive $(000\bar{1})$ surface typically does not grow nanobelt structures. The self-catalyzed process is likely a mechanism for the growth of nanobelts without the presence of foreign metallic catalysts. The nanocantilever arrays have potential applications as nanoscale sensor arrays and tweezer arrays.

CONCLUDING REMARKS AND PERSPECTIVES

This article reviews the novel nanobelt-based nanostructures of functional oxides. Among the group of ZnO, SnO_2, In_2O_3, Ga_2O_3, CdO, and PbO_2, which belong to different crystallographic systems and structures, a generic shape of nanobelt structure has been preserved. The nanobelts are single crystalline and free from dislocation, and their surfaces are atomically flat. These are truly structurally controlled quasi-one-dimensional nanomaterials for nanotechnology. The nanobelts can be a template for synthesis of novel materials and complex structures. The oxides are intrinsic semiconductors, which have been used for fabrication of nanosize functional devices such as field-effect transistors and gas sensors, nanoresonators,

and nanocantilevers. These devices will have important applications in nanosystems and biotechnology.

Growth of (0001) facets–dominated, freestanding, and piezoelectric zinc oxide (ZnO) nanostructures is challenged by the divergence of the surface energy due to intrinsic polarization. Very recently, structurally controlled nanobelts exhibiting piezoelectric and ferroelectric properties have been synthesized, and could be candidates for nanoscale traducers, actuators, and sensors. By controlling growth kinetics, we show the success of growing nanobelt-based novel structures whose surfaces are dominated by the polarized $\pm(0001)$ facets. Owing to the positive and negative ionic charges on the zinc- and oxygen-terminated $\pm(0001)$ surfaces, respectively, a spontaneous polarization is induced across the nanobelt thickness. As a result, helical nanostructures and nanorings are formed by rolling up single-crystal nanobelts; this phenomenon is attributed to minimizing the total energy contributed by spontaneous polarization and elasticity. The polar surface–dominated ZnO nanobelts are likely to be an ideal system for understanding piezoelectricity and polarization-induced ferroelectricity at nanoscale and they could have applications as one-dimensional nanoscale sensors, transducers, and resonators.

The nanobelts and relevant nanostructures are a unique group that is likely to have important applications in nanosize electronic, optical, sensor, and optoelectronic devices. As for the future of nanotechnology and applications in nanosystems and biotechnology, there are a lot of issues to be investigated:

1. For sensor applications, the nanobelts may have the required sensitivity, but the selectivity needs to be improved. This requires the synthesis of composite nanobelts such as heterostructure, junction, and barrier. Exploration of complex oxides involving two or more types of cations is needed to improve their multifunctionality. Surface functionalization of the nanobelts is also an important topic.
2. Controlled growth is required to control nanobelts' size, size distribution, shape, crystal structure, defect distribution, and even surface structure (atomic termination, surface polarization). A thorough understanding of the growth mechanism is the key. In processing, a valid way to control the size of nanobelts is to properly control the temperature, pressure, and growth time.
3. Techniques are required to grow nanobelts into aligned arrays, onto patterned substrates, and in self-assembly structures with functionality. This is a key step toward nanosystem integration.
4. Finally, development of techniques for integration of nanobelts with other nano- and microstructures such as nanoelectromechanical and biosensing systems is needed.

ACKNOWLEDGMENT

The results reviewed in this paper were partially contributed by my group members and collaborators: Xiangyang Kong, Puxian Gao, Xuedong Bai, Carsten Ronning, Zhengwei Pan, Jing Li, William Hughes, Daniel Moore, Chris Ma, Xudong Wang,

Yolande Berta, Li Shi, Zhen Yao, M.S. Arnold, Ph. Avouris, E. Comini, G. Faglia, G. Sberveglieri, and Enge Wang, to whom I am very grateful. Research was supported by NSF, NASA, and NSFC.

The *Annual Review of Physical Chemistry* is online at http://physchem.annualreviews.org

LITERATURE CITED

1. Wang ZL, ed. 2003. *Nanowires and Nanobelts*, Vol. I. *Metal and Semiconductor, Nanowires*. New York: Kluwer Academic
2. Wang ZL, ed. 2003. *Nanowires and Nanobelts*, Vol. II. *Nanowires and Nanobelts of Functional Materials*, New York: Kluwer Academic
3. Iijima S. 1991. *Nature* 354:56–58
4. Rothschild A, Sloan J, Tenne R. 2000. *J. Am. Chem. Soc.* 122:5169–79
5. Tenne R, Homyonfer M, Feldman Y. 1998. *Chem. Mater*. 10:3225–38
6. Saito Y, Matsumoto T. 1998. *Nature* 392:237–37
7. Gao PX, Wang ZL. 2003. *J. Am. Chem. Soc.* 125:11299–305
8. Trentler TJ, Hickman KM, Goel SC, Viano AM, Gibbons PC, Buhro WE. 1995. *Science* 270:1791–94
9. Morales AM, Lieber CM. 1998. *Science* 279:208–11
10. Lee ST, Wang N, Zhang YF, Tang YH. 1999. *MRS Bull.* 24:36–42
11. Chen CC, Yeh CC, Chen CH, Yu MY, Liu HL, et al. 2001. *J. Am. Chem. Soc.* 123:2791–98
12. Pan ZW, Dai ZR, Ma C, Wang ZL. 2002. *J. Am. Chem. Soc.* 124:1817–22
13. Dai HJ, Wong EW, Lu YZ, Fan SS, Lieber CM. 1995. *Nature* 375:769–72
14. Manna L, Scher EC, Alivisatos AP. 2000. *J. Am. Chem. Soc.* 122:12700–6
15. Huang MH, Wu YY, Feick H, Tran N, Weber E, Yang PD. 2001. *Adv. Mater.* 13:113–16
16. Lao JY, Huang JY, Wang DZ, Ren ZF. 2003. *Nano Lett.* 3:235–38
17. Zhang Y, Suenaga K, Colliex C, Iijima S. 1998. *Science* 281:973–75
18. Wang ZL, Dai ZR, Gao RP, Bai ZG, Gole JL. 2000. *Appl. Phys. Lett.* 77:3349–51
19. Pan ZW, Dai ZR, Wang ZL. 2001. *Science* 291:1947–50
20. Wang ZL, Pan ZW, Dai ZR. 2003. US Patent No. 6,586,095
21. Dai ZR, Pan ZW, Wang ZL. 2002. *J. Phys. Chem. B* 106:902–4
22. Dai ZR, Pan ZW, Wang ZL. 2002. *J. Am. Chem. Soc.* 124:8673–80
23. Wang ZL, Kang ZC. 1998. *Functional and Smart Materials*. New York: Plenum
24. Frankfutter Allgemeine Zeitung, June 3, 2003
25. Wen XG, Zhang WX, Yang SH. 2002. *Nano Lett.* 2:1397–401
26. Li YB, Bando Y, Golberg D, Kurashima K. 2002. *Appl. Phys. Lett.* 81:5048–50
27. Zhou J, Xu NS, Deng SZ, Chen J, She JC, Wang ZL. 2003. *Adv. Mater.* 15:1835–40
28. Li YB, Bando Y, Sato T. 2002. *Chem. Phys. Lett.* 359:141–45
29. Liu J, Cai J, Son YC, Gao QM, Suib SL, Aindow M. 2002. *J. Phys. Chem. B* 106:9761–68
30. Wen XG, Zhang WX, Yang SH. 2003. *Langmuir* 19:5898–903
31. Dai ZR, Pan ZW, Wang ZL. 2001. *Solid State Commun*. 118:351–54
32. Dai ZR, Gole JL, Stout JD, Wang ZL. 2002. *J. Phys. Chem. B* 106:1274–79
33. Dai ZR, Pan ZW, Wang ZL. 2003. *Adv. Funct. Mater.* 13:9–24
34. Kong XY, Wang ZL. 2003. *Solid State Commun*. 128:1–4

35. Li C, Zhang D, Han S, Liu X, Tang T, Zhou C. 2003. *Adv. Mater.* 15:143–46
36. Dai ZR, Pan ZW, Wang ZL. 2002. *J. Phys. Chem. B.* 106:902–4
37. Pan ZW, Dai ZR, Wang ZL. 2002. *Appl. Phys. Lett.* 80:309–11
38. Ma C, Moore D, Li J, Wang ZL. 2003. *Adv. Mater.* 15:228–31
39. Shi W, Peng H, Wang N, Li CP, Xu L, et al. 2001. *J. Am. Chem. Soc.* 123:11095–96
40. Gao PX, Wang ZL. 2002. *J. Phys. Chem. B* 106:12653–58
41. Wen JG, Lao JY, Wang DZ, Kyaw TM, Foo YL, Ren ZF. 2003. *Chem. Phys. Lett.* 372:717–22
42. He RR, Law M, Fan R, Kim F, Yang PD. 2002. *Nano Lett.* 2:1109–12
43. Kong XY, Ding Y, Wang ZL. 2004. *J. Phys. Chem.* 108:570–74
44. Ding Y, Kong XY, Wang ZL. 2003. *J. Appl. Phys.* 95:306–10
45. Sun YG, Mayers B, Xia YN. 2003. *Nano Lett.* 3:675–79
46. Wang XD, Li J, Gao PX, Summers CJ, Wang ZL. 2002. *Adv. Mater.* 14:1732–35
47. Wolf SA, Awschalom DD, Buhrmann RA, Daughton JM, von Molnar S, et al. 2001. *Science* 294:1488–95
48. Prinz GA. 1998. *Science* 282:1660–63
49. Dietl T, Ohno H, Matsukura F, Cibert J, Ferrand D. 2000. *Science* 287:1019–22
50. Ronning C, Gao PX, Ding Y, Wang ZL, Schwen D. 2003. *Appl. Phys. Lett.* In press
51. Huang MH, Wu Y, Feick H, Tran N, Weber E, Yang P. 2001. *Adv. Mater.* 13:113–16
52. Gao PX, Ding Y, Wang ZL. 2003. *Nano Lett.* 3:1315–20
53. Arnold SM, Kounce SE. 1956. *J. Appl. Phys.* 27:964–66
54. Frank FC. 1949. *Discus. Faraday Soc.* 5:48–54
55. Wagner RS, Ellis WC. 1964. *Appl. Phys. Lett.* 4:89–91
56. Duan XF, Lieber CM. 2000. *Adv. Mater.* 12:298–302
57. Yu DP, Xing YJ, Hang QL, Yan HF, Xu J, et al. 2001. *Physica E* 9:305–9
58. Choi YC, Kim WS, Park YS, Lee SM, Bae DJ, et al. 2000. *Adv. Mater.* 12:746–50
59. Han WQ, Kohler-Redlich P, Ernst F, Rühle M. 2000. *Solid State Commun.* 115:527–29
60. Liang C, Meng G, Lei Y, Phillipp F, Zhang L. 2001. *Adv. Mater.* 13:1330–33
61. Holmes JD, Johnston KP, Doty RC, Korgel BA. 2000. *Science* 287:1471–73
62. Wang N, Tang YH, Zhang YF, Lee CS, Bello I, Lee ST. 1999. *Chem. Phys. Lett.* 299:237–42
63. Yin Y, Zhang G, Xia Y. 2002. *Adv. Funct. Mater.* 12:293–298
64. Yang PD, Lieber CM. 1997. *J. Mater. Res.* 12:2981–96
65. Wang YW, Liang CH, Meng GW, Peng XS, Zhang LD. 2002. *J. Mater. Chem.* 12:651–53
66. Wang ZL, Gao RP, Gole JL, Stout JD. 2000. *Adv. Mater.* 12:1938–41
67. Cabrera N, Burton WK. 1949. *Discus. Faraday Soc.* 5:40–48
68. Sears GW. 1955. *Acta Metall.* 3:361–66
69. Blakely JM, Jackson KA. 1962. *J. Chem. Phys.* 37:428–30
70. Wang ZL, Kong XY, Zuo JM. 2003. *Phys. Rev. Lett.* 91:185502
71. Morrison SR. 1982. *Sens. Actuators* 2:329–36
72. Sharma RK, Chan PCH, Tang Z, Yan G, Hsing IM, Sin JKO. 2001. *Sens. Actuators B* 72:160–66
73. Hahn SH, Barsan N, Weimar U. 2001. *Sens. Actuators B* 78:64–68
74. Lin HM, Tzeng SJ, Hsiau PJ, Tsai WL. 1998. *NanoStr. Mater.* 10:465–77
75. Arnold MS, Avouris Ph, Pan ZW, Wang ZL. 2003. *J. Phys. Chem. B* 107:659–63
76. Cui Y, Lieber CM. 2001. *Science* 291: 851–54
77. Collins PG, Arnold MS, Avouris Ph. 2001. *Science* 292:706–9
78. Kong J, Franklin N, Wu C, Pan S, Cho KJ, Dai H. 2000. *Science* 287:622–25
79. Avouris Ph. 2002. *Chem. Phys.* 281:429–45
80. Advani GN, Kluge-Weiss P, Longini RL,

Jordan AG. 1980. *Int. J. Electron.* 48:403–11
81. Samson S, Fonstad CG. 1973. *J. Appl. Phys*. 44:4618–21
82. Kamp B, Merkle R, Maier J. 2001. *Sens. Actuators B* 77:534–42
83. Göpel W, Schierbaum K, Wiemhöfer HD. 1989. *Solid State Ionics* 32:440–50
84. Mizusaki J, Koinuma H, Shimoyama JI, Kawasaki M, Fueki K. 1990. *J. Solid State Chem*. 88:443–50
85. Zhang DH. 1996. *Mater. Chem. Phys.* 45:248–52
86. Bonasewicz P, Hirschwald W, Neumann G. 1986. *J. Electrochem. Soc.* 133:2270–78
87. Shapira Y, Cox SM, Lichtma D. 1976. *Surf. Sci.* 54:43–59
88. Bai XD, Wang EG, Gao PX, Wang ZL. 2003. *Nano. Lett.* 3:1147–50
89. Comini E, Faglia G, Sberveglieri G, Pan ZW, Wang ZL. 2002. *Appl. Phys. Lett.* 81:1869–71
90. Kim P, Shi L, Majumdar A, McEuen PL. 2001. *Phys. Rev. Lett.* 87:215502–5
91. Schwab K, Henriksen EA, Worlock JM, Roukes ML. 2000. *Nature* 404:974–77
92. Shi L, Hao Q, Yu C, Kim D, Mingo N, et al. 2003. *Appl. Phys. Lett.* Submitted
93. Volz SG, Chen G. 1999. *Appl. Phys. Lett.* 75:2056–58
94. Sverdrup PG, Ju YS, Goodson KE. 2001. *J. Heat Transf.* 123:130–36
95. Poncharal P, Wang ZL, Ugarte D, de Heer WA. 1999. *Science* 283:1513–16
96. Wang ZL, Poncharal P, de Heer WA. 2000. *Pure Appl. Chem.* 72:209–19
97. Gao RP, Wang ZL, Bai ZG, de Heer WA, Dai LM, Gao M. 2000. *Phys. Rev. Lett.* 85:622–25
98. Meirovich L. 1986. *Elements of Vibration Analysis*. New York: McGraw-Hill. 2nd ed.
99. Bai XD, Wang EG, Gao PX, Wang ZL. 2003. *Appl. Phys. Lett.* 82:4806–8
100. Gao RP, Pan ZW, Wang ZL. 2001. *Appl. Phys. Lett.* 78:1757–59
101. Bai XD, Wang EG, Gao PX, Wang ZL. 2003. *Nano Lett.* 3:1147–50
102. Dai HJ, Hafner JH, Rinzler AG, Colbert DT, Smalley RE. 1996. *Nature* 384:147–50
103. Hughes W, Wang ZL. 2003. *Appl. Phys. Lett.* 82:2886–88
104. Dulub O, Boatner LA, Diebold U. 2002. *Surf. Sci.* 519:201–17
105. Meyer B, Marx D. 2003. *Phys. Rev. B* 67:035403-1–11
106. Tasker PW. 1979. *J. Phys. C: Solid State Phys.* 12:4977–84
107. Dulub O, Diebold U, Kresse G. 2003. *Phys. Rev. Lett.* 90:016102
108. Wander A, Schedin F, Steadman P, Norris A, McGrath R, et al. 2001. *Phys. Rev. Lett.* 86:3811–14
109. Staemmler V, Fink K, Meyer B, Marx D, Kunat M, et al. 2003. *Phys. Rev. Lett.* 90:106102–1
110. Dal Corso A, Posternak M, Resta R, Baldereschi A. 1994. *Phys. Rev. B* 50:10715–21
111. Bernardini F, Fiorentini V, Vanderbilt D. 1997. *Phys. Rev. B* 56:10024–27
112. Kong XY, Wang ZL. 2003. *Nano Lett.* 3:1625–31
113. Amelinckx S, Zhang XB, Bernaerts D, Zhang XF, Ivanov V, Nagy JB. 1994. *Science* 265:635–39
114. Martel R, Shea HR, Avouris P. 1999. *Nature* 398:299
115. Sano M, Kamino A, Okamura J, Shinkai J. 2001. *Science* 293:1299–301
116. Zhang HF, Wang CM, Wang LS. 2002. *Nano Lett.* 2:941–44
117. Gao RP, Wang ZL, Fan SS. 2000. *J. Phys. Chem. B* 104:1227–34
118. Tian ZR, Voigt JA, Liu J, Mckenzie B, Mcdermott MJ. 2002. *J. Am. Chem. Soc.* 124:12954–55
119. Hashimoto S, Yamaguchi A. 1996. *J. Am. Ceram. Soc.* 79:1121

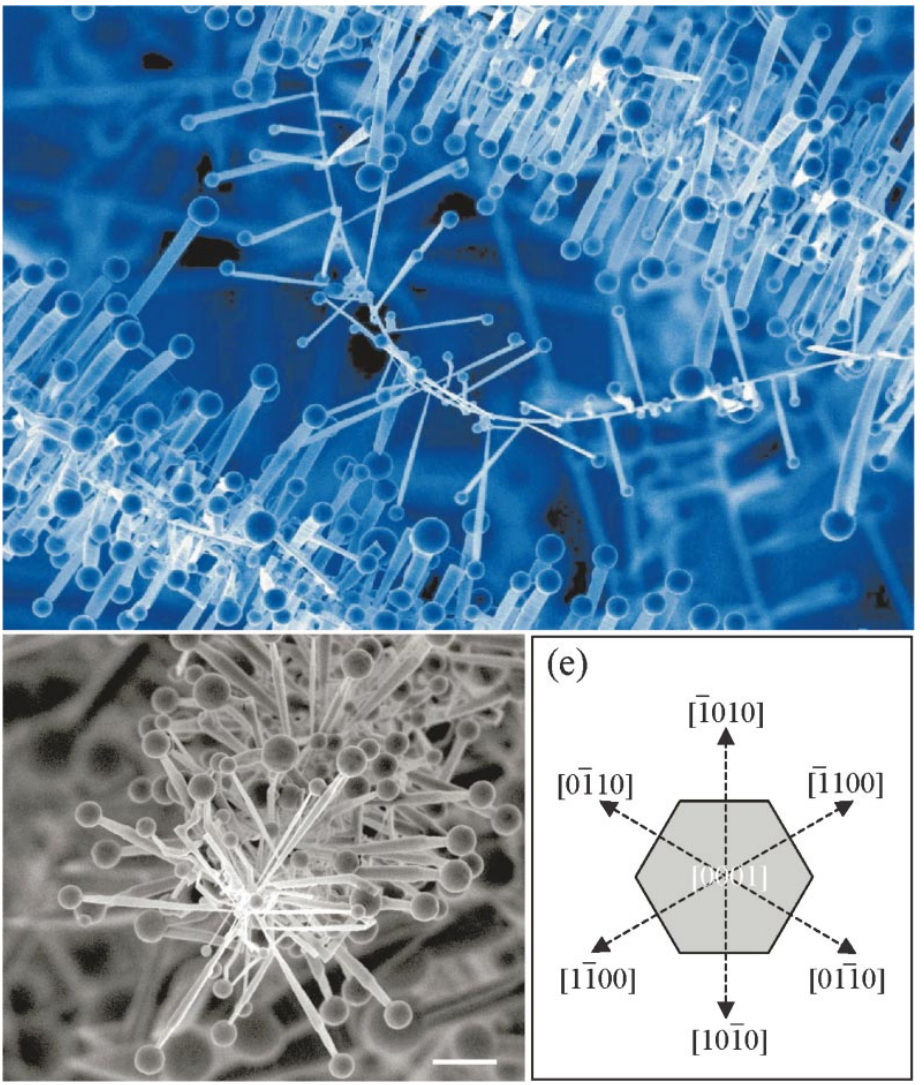

Figure 7 (*a*,*b*) SEM images of the hierarchical ZnO nanowire-nanobelt junction arrays grown using Sn catalyst. (*c*) Growth model of the hierarchical structure.

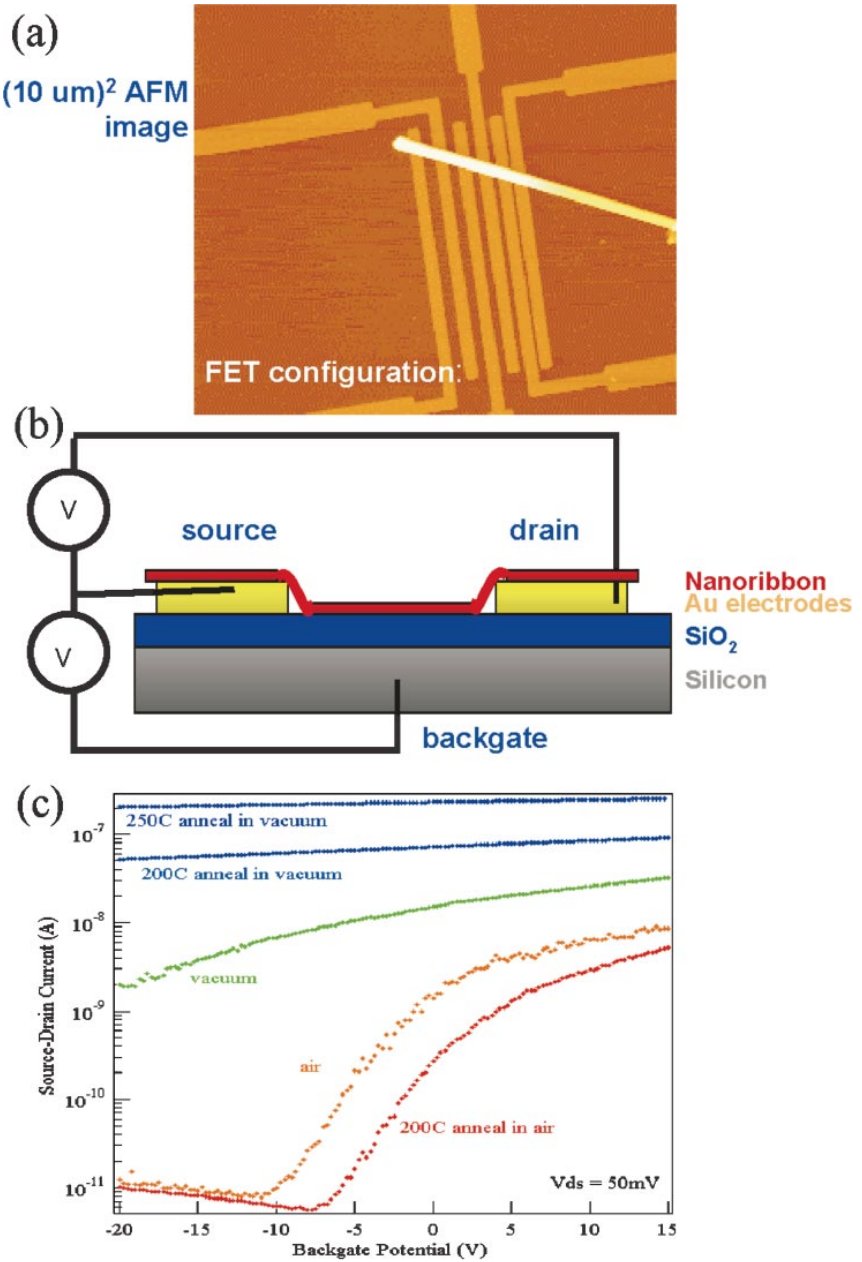

Figure 14 (*a*) Atomic force microscopy image of a field-effect transistor (FET) device made using a single nanobelt. (*b*) Schematic working diagram of the device. (*c*) SnO_2 nanobelt FET oxygen sensitivity. Source-drain current versus gate bias for a SnO_2 FET after various treatments was measured in this order: air, vacuum, 200°C vacuum anneal, 250°C vacuum anneal, 200°C air anneal.

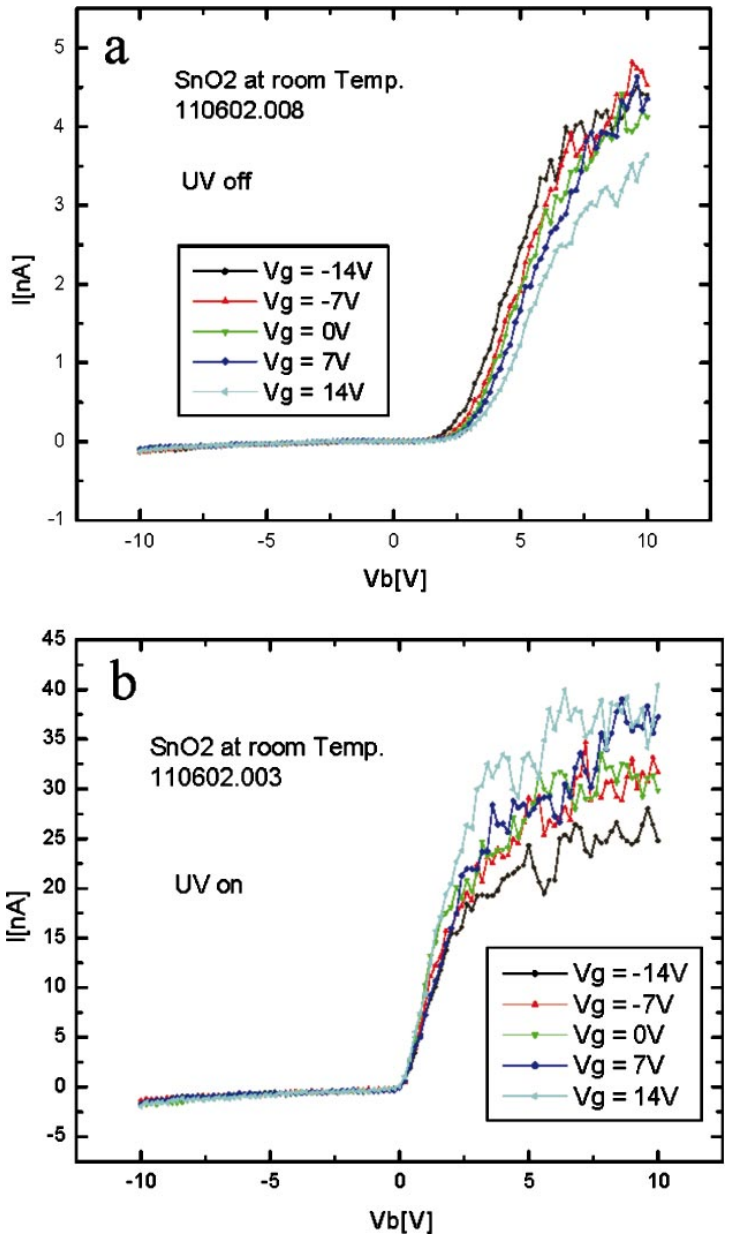

Figure 15 Solid state diode of a single nanobelt. The current versus voltage (I–V) characteristic curves of a diode made using a single SnO_2 nanobelt, showing its response to gate voltage (*a*) without and (*b*) with UV radiation (figure provided by Prof. Zhen Yao, University of Texas Austin).

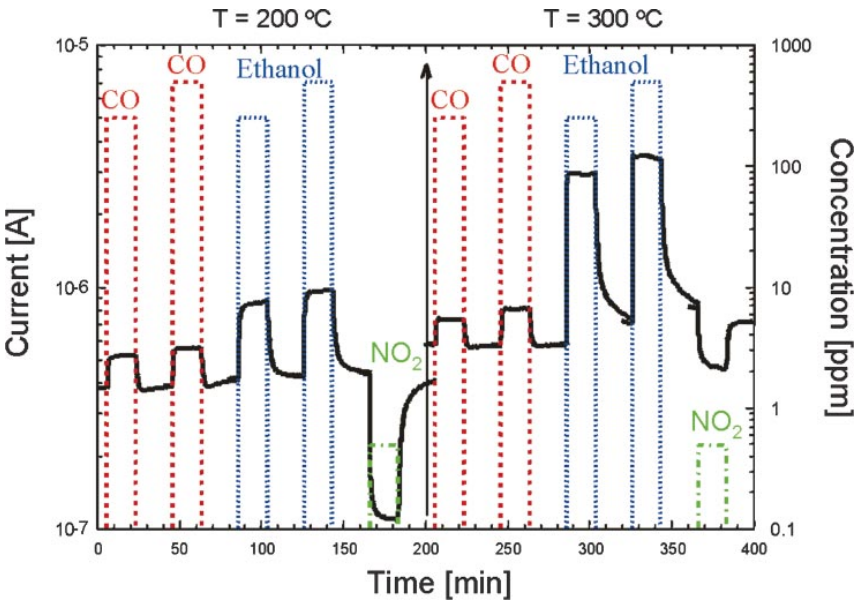

Figure 16 Gas sensors made using nanobelts. Response of the conductance through SnO_2 nanobelts to the concentration of the surface-adsorbed CO, ethanol, and NO_2 gases at two different temperatures.